

A new WENO-based momentum advection scheme for simulations of ocean mesoscale turbulence

Simone Silvestri¹, Gregory L. Wagner¹, Jean-Michel Campin¹,
 Navid C. Constantinou², Christopher N. Hill¹, Andre Souza¹,
 and Raffaele Ferrari¹

¹Massachusetts Institute of Technology, Cambridge, MA, USA

²Australian National University, Canberra, ACT, Australia

Key Points:

- We describe a new momentum advection scheme based on upwind-biased, weighted essentially non-oscillatory (WENO) reconstructions.
- The new scheme automatically adapts to horizontal resolution without generating grid-scale noise typical of low order oscillatory schemes.
- The new scheme delivers a higher “effective” resolution compared to other diffusive schemes as well as a second-order scheme stabilized by standard explicit dissipation methods.

Abstract

Current eddy-permitting and eddy-resolving ocean models require dissipation to prevent a spurious accumulation of enstrophy at the grid scale. We introduce a new numerical scheme for momentum advection in large-scale ocean models that involves upwinding through a weighted essentially non-oscillatory (WENO) reconstruction. The new scheme provides implicit dissipation and thereby avoids the need for an additional explicit dissipation that may require calibration of unknown parameters. This approach uses the rotational, “vector invariant” formulation of the momentum advection operator that is widely employed by global general circulation models. A novel formulation of the WENO “smoothness indicators” is key for avoiding excessive numerical dissipation of kinetic energy and enstrophy at grid-resolved scales. We test the new advection scheme against a standard approach that combines explicit dissipation with a dispersive discretization of the rotational advection operator in two scenarios: (*i*) two-dimensional turbulence and (*ii*) three-dimensional baroclinic equilibration. In both cases, the solutions are stable, free from dispersive artifacts, and achieve increased “effective” resolution compared to other approaches commonly used in ocean models.

Plain Language Summary

High-resolution climate models that resolve the cyclones and anticyclones in the ocean, often called “eddies”, must prevent an artificial build-up of whirl-like movements, or “enstrophy”, at the model’s grid-scale. But even though methods that prevent artificial accumulation of enstrophy are included only to ensure numerical stability, they unfortunately also negatively impact the quality of the model predictions even at scales larger than the grid-scale. Here, we devise a novel numerical method to overcome this deficiency. Our method has the best of both worlds: it removes just enough enstrophy so that the flow is as close to reality as possible and it achieves this without accumulating enstrophy at grid-scale.

Corresponding author: Simone Silvestri, silvestri.simone0@gmail.com

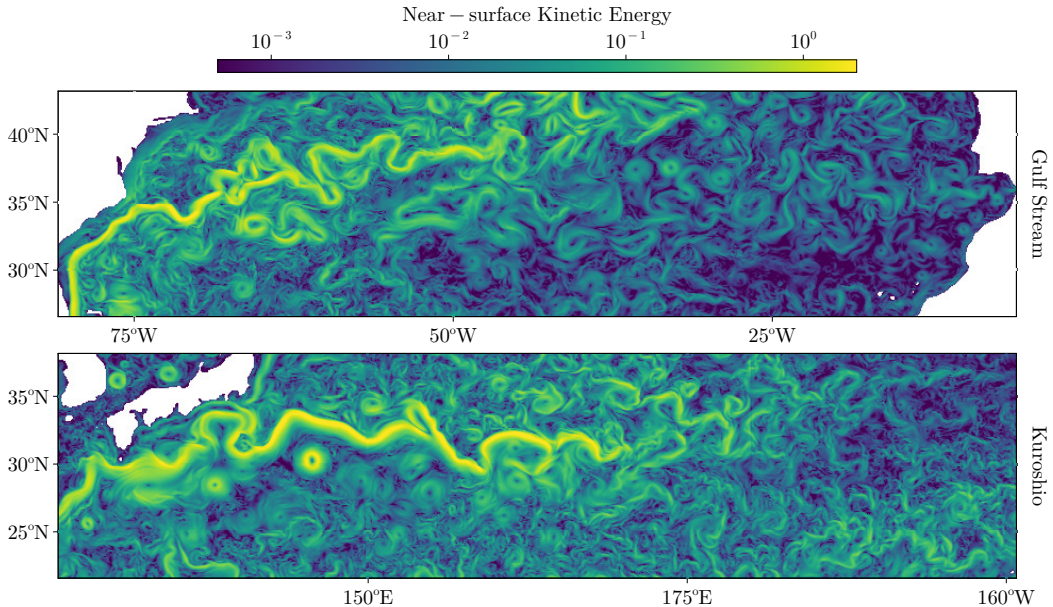


Figure 1. Near-surface kinetic energy in the Gulf stream (top panel) and the Kuroshio current (bottom panel) on March 1st from a global ocean simulation at 1/12-th of a degree horizontal resolution and 100 vertical levels that uses the novel advection scheme we introduce here as a momentum closure.

1 Introduction

Mesoscale ocean turbulence, characterized by eddies ranging from 10 to 100 kilometers in size, plays a crucial role in mixing heat, salt, momentum, and biogeochemical tracers throughout the ocean. This mixing in turns exerts a leading-order control on the large-scale ocean circulation and its impact on climate (Vallis, 2017). Until recently, climate models used ocean grids coarser than 100 km and resorted to parameterize this turbulence. The existing parameterizations (Gent & Mcwilliams, 1990) remain quite uncertain and contribute significant uncertainties to climate projections. In the last few years it has become possible to run global ocean simulations with fine grids in the 10–25 km range that partially resolve the mesoscale turbulence. This resolution is referred to as “eddy-permitting” in contrast to the “eddy-resolving” resolution that requires even finer grids, beyond presently available computational resources for climate projections (Ding et al., 2022; Silvestri et al., 2023). The eddy-permitting regime shares conceptual similarities with the well-established Large Eddy Simulation (LES) technique used in computational fluid dynamics for three-dimensional turbulence. In both cases, the grid resolution resolves only the largest turbulent eddies. The goal of this paper is to exploit this similarity and develop an accurate numerical scheme for mesoscale turbulence.

Numerical schemes for momentum advection can be categorized into two types based on the numerical characteristics of the leading order truncation term: *dispersive* and *diffusive*. Global ocean models typically rely on dispersive schemes and mitigate the dispersive “noise” by adding explicit diffusive closures (Adcroft et al., 2019; Su et al., 2018). These closures range from simple laplacian/bilaplacian diffusion with static viscosity (Schwarzkopf et al., 2019; Li et al., 2020) to more complex dynamical viscosities inspired by Large Eddy Simulations (LES) (Smagorinsky, 1963; Fox-Kemper & Menemenlis, 2004; Bachman et al., 2017). Conversely, diffusive numerical schemes exhibit a leading order diffusive error that ensures stability, eliminating the need for additional explicit closures. Examples of such schemes include flux-limited advection (Van Leer, 1977; Zalesak, 1979), piecewise-parabolic methods (Woodward

& Colella, 1984; Sytine et al., 2000), semi-Lagrangian advection (Bates & McDonald, 1982), and essentially non-oscillatory schemes (Osher & Shu, 1991).

A major advantage of diffusive numerical schemes is that they avoid a key drawback of explicit closures: the need to calibrate unknown free parameters to adapt to resolution. As importantly, they suppress spurious numerical modes caused by dispersion errors typical of centered reconstruction schemes. Explicit closures, instead, often require additional tweaking to dampen spurious computational modes as will be illustrated in idealized test cases. This reduces the effective resolution of the simulation, because the smallest scales are compromised by numerics, and may even affect the accuracy of the large-scale solutions since the mesoscale regime is characterized by a vigorous inverse energy cascade (Pressel et al., 2017).

A disadvantage of diffusive schemes is that momentum diffusion is built in the numerical reconstruction, rather than explicitly prescribed. Thus the overall dissipation cannot be easily controlled and can exceed that of explicit closures. To avoid this, the reconstruction schemes must be designed to minimize energy dissipation by utilizing stencils of sufficiently high order. Another notable drawback of implicit diffusion is that assessing energy budgets is more complicated than with energy-conserving dispersive methods stabilized by explicit dissipation. Hence, the choice of a diffusive method over a dispersive approach requires substantial evidence of significant accuracy benefits.

In this paper, we introduce a novel diffusive numerical scheme designed to reduce both the energy dissipation and the noise at the grid scale, thereby increasing the effective resolution of the model and improving numerical stability. Importantly, the new scheme holds the promise to reduce the computational cost of “eddy-resolving” ocean simulations which could be achieved with coarser grids than with presently used schemes.

Diffusive numerical schemes has seen application in various computational fluid dynamics fields, especially in combination with the conservative (or “flux-form”) formulation of the advection operator (Karaca et al., 2012; Maulik & San, 2018; Zeng et al., 2021), including in atmospheric models (Smolarkiewicz & Margolin, 1998; Souza et al., 2023; Norman et al., 2023) and regional ocean models (Shchepetkin & McWilliams, 1998a; Holland et al., 1998; Mohammadi-Aragh et al., 2015). However, finite-volume general circulation models (GCMs) often favor the rotational formulation of the advection operator due to its ease of implementation with non-regular grids, such as the cubed sphere grid (Ronchi et al., 1996), the latitude-longitude capped grid (Fenty & Wang, 2020), or the tripolar grid (Madec & Imbard, 1996). Within the rotational framework, the application of upwinding-based numerical schemes is far less common. Hahn and Iaccarino (2008) introduced upwinding in the rotational three-dimensional Navier–Stokes equations applied to the kinetic energy gradient, while Ringler (2011) described the upwinding of vorticity in the vorticity flux term as a possible monotone, diffusive discretization of the advection operator in the rotational form. The latter approach, which aligns more with the intrinsic dynamics of two-dimensional flows that are characterized by a forward enstrophy cascade, has been implemented by Roullet and Gaillard (2022) in the rotational form of the shallow-water equations using a weighted essentially non-oscillatory (WENO) reconstruction scheme.

Despite this recent progress, a mature formulation of a rotational-based upwind-biased numerical scheme for the primitive equations¹ solved by GCMs, is still lacking. Here, we take inspiration from Roullet and Gaillard (2022) and develop a WENO reconstruction scheme tailored to the rotational formulation of the advection operator, applicable to both the two-dimensional Navier–Stokes and the primitive equations. We propose this scheme as an alternative to the commonly used approach for tackling mesoscale turbulence in eddy-permitting ocean simulations, which employs explicit viscous closures paired with low-order

¹ The Navier-Stokes equations under the hydrostatic approximation are referred to as the primitive equations in the atmospheric and ocean modeling literature.

115 oscillatory (dispersive) advection schemes (Adcroft et al., 2019; Ding et al., 2022). Our
 116 method is constructed with two objectives in mind: (i) ensuring stability through variance
 117 dissipation of both rotational and divergent motions, eliminating the need for additional
 118 explicit dissipation, and (ii) controlling the implicit numerical diffusion through a novel
 119 approach to smoothness metrics in the WENO framework. The outcome is a method that
 120 delivers a higher “effective” resolution of the mesoscale turbulent spectra in eddy-permitting
 121 ocean simulations when compared to the approaches tested in this paper. Figure 1 shows
 122 snapshots of the surface kinetic energy from a global ocean simulation run at the “eddy
 123 permitting” lateral resolution of 1/12th degree using the novel method. The solution is
 124 characterized by a rich web of well-resolved sharp jets without grid-scale noise. We will show
 125 that traditional explicit schemes generate much noisier solutions at the grid-scale at the
 126 same resolution.

127 The paper is organized as follows. In section 2 we derive the new formulation of the
 128 rotational advection operator that lends itself to a diffusive discretization. In section 3,
 129 we describe the WENO reconstruction scheme and show how it can be applied to fluxed
 130 quantities in the context of the rotational form of the primitive equations. We test our newly
 131 defined WENO reconstruction in the context of two-dimensional decaying turbulence in
 132 section 4 and, finally, in section 5 we test the new rotational-based advection operator as a
 133 momentum closure alternative in an idealized baroclinic jet case. We conclude with some
 134 discussion in section 6.

135 2 An upwinding approach applied to the rotational form of the primitive 136 equations

137 Ocean mesoscale turbulence is characterized by an inverse cascade of energy from small
 138 to large scales, weak energy dissipation, and a forward cascade of enstrophy terminated by
 139 enstrophy dissipation at small scales. Typical finite-volume discretizations of the primitive
 140 equations generate oscillatory noise at small scales that must be countered with explicit
 141 dissipation, typically via an empirical hyperviscosity. The objective of this section is to
 142 explore an alternative discretization of the primitive equations that is inherently diffusive
 143 and therefore does not generate oscillatory grid-scale noise. Specifically, we propose a
 144 discretization that effectively diffuses vorticity and horizontal divergence, enabling precise
 145 control of the dissipation of both rotational and divergent modes.

146 2.1 High-level description of the upwinding strategy

147 To provide an introductory sketch of our discretization, consider the rotational form of
 148 the advective terms in the horizontal momentum equations,

$$149 D_t u = \underbrace{\partial_t u}_{\text{time derivative}} + \underbrace{\zeta v}_{\text{vorticity flux}} - \underbrace{w \partial_z u}_{\text{vertical advection}} - \underbrace{\partial_x K}_{\text{kinetic energy gradient}}, \quad (1)$$

$$150 D_t v = \underbrace{\partial_t v}_{\text{time derivative}} - \underbrace{\zeta u}_{\text{vorticity flux}} - \underbrace{w \partial_z v}_{\text{vertical advection}} - \underbrace{\partial_y K}_{\text{kinetic energy gradient}}, \quad (2)$$

151 where u, v are the horizontal velocity components, $\zeta \stackrel{\text{def}}{=} \partial_x v - \partial_y u$ is the vertical vorticity,
 152 and $K \stackrel{\text{def}}{=} \frac{1}{2} (u^2 + v^2)$ is the horizontal kinetic energy. Mass conservation is enforced by the
 153 continuity equation for an incompressible fluid like seawater,
 154

$$155 \underbrace{\partial_x u + \partial_y v}_{\stackrel{\text{def}}{=} d} = -\partial_z w, \quad (3)$$

156 where we have defined the horizontal divergence, d .

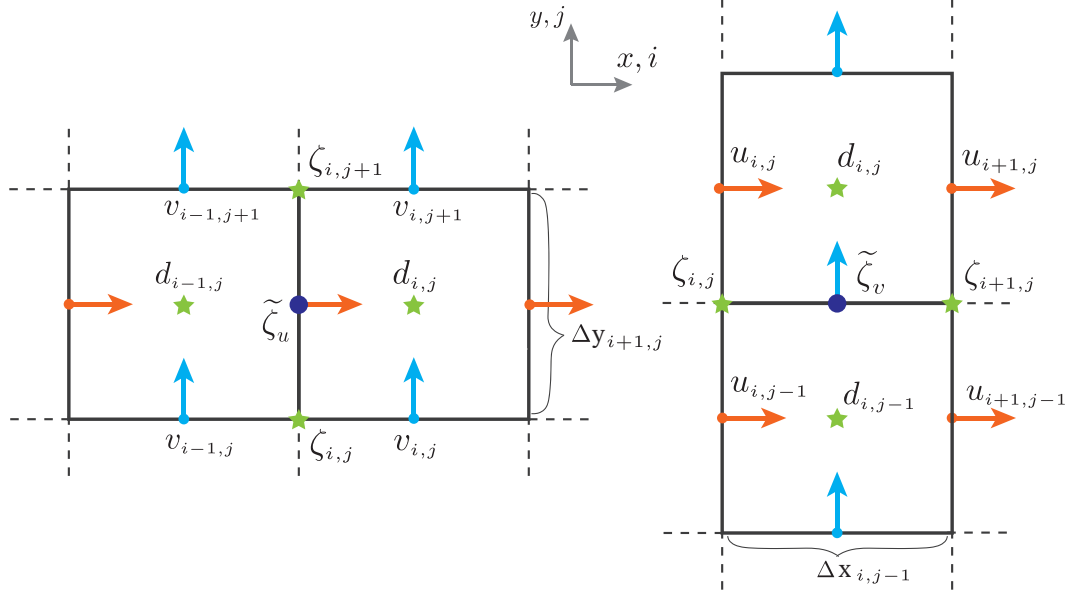


Figure 2. A sketch showing the variables' relative location on a staggered C-grid. Red and blue arrows denote the location of u - and v -velocity components, respectively; green stars show the location of vertical vorticity and horizontal divergence. Purple circles (ζ_u and ζ_v) are the *average* vorticities required to calculate the vorticity flux at u locations (left) and at v locations (right).

To lighten the notation we outline our discretization on a horizontally-isotropic rectilinear grid with regular horizontal spacing Δ . The discretization follows the staggered C-grid finite volume approach shown in Arakawa and Lamb (1977). A simplified representation of the variables' relative location on the discrete grid is shown in figure 2.

We use the vorticity flux to exemplify the numerical error associated with the widely used momentum advection schemes in computational oceanography. In a finite volume framework, it is customary to approximate the cell-averaged vorticity flux as the product of the average vorticity and the averaged velocity. An “enstrophy-conserving” (Arakawa, 1966) discretization on a C-grid requires the *reconstruction* of average vorticity at the velocity locations (see figure 2) where ζ_u and ζ_v express the *true* value of vorticity averaged in the volumes corresponding to velocity locations. Using a centered second-order approximation, denoted here with angle brackets:

$$\zeta_u \approx \langle \zeta \rangle^j \stackrel{\text{def}}{=} \frac{\zeta_{i,j+1} + \zeta_{i,j}}{2}, \text{ for use in } \zeta v, \quad (4)$$

$$\zeta_v \approx \langle \zeta \rangle^i \stackrel{\text{def}}{=} \frac{\zeta_{i+1,j} + \zeta_{i,j}}{2}, \text{ for use in } \zeta u. \quad (5)$$

We compute the numerical error \mathcal{N}_ζ by assuming that Δ is small and performing a Taylor expansion

$$\zeta_{i,j+1} = \zeta_u + \frac{\Delta}{2} \partial_y \zeta + \frac{\Delta^2}{8} \partial_y^2 \zeta + \frac{\Delta^3}{48} \partial_y^3 \zeta + \mathcal{O}(\Delta^4), \quad (6)$$

$$\zeta_{i,j} = \zeta_u - \frac{\Delta}{2} \partial_y \zeta + \frac{\Delta^2}{8} \partial_y^2 \zeta - \frac{\Delta^3}{48} \partial_y^3 \zeta + \mathcal{O}(\Delta^4), \quad (7)$$

where

$$\frac{\zeta_{i,j+1} + \zeta_{i,j}}{2} = \zeta_u + \mathcal{N}_\zeta, \quad \text{with} \quad \mathcal{N}_\zeta = \frac{\Delta^2}{8} \partial_y^2 \zeta + \mathcal{O}(\Delta^4). \quad (8)$$

In the same way, a centered discretization of the y -momentum vorticity flux leads to $\mathcal{N}_\zeta \sim \Delta^2 \partial_x^2 \zeta$ in (2). This truncation error is proportional to an even derivative of the vorticity field and therefore an odd derivative of the momentum field, acting as an additional

182 spurious dispersion term in the momentum equations. By constructing $\partial_x(2) - \partial_y(1)$, we
 183 can see that the same error is dispersive also in the vorticity evolution equation and leads to
 184 additional numerical rotational modes.

185 The vorticity flux is not the only term that leads to dispersion, the same analysis
 186 (not done here) shows that a centered reconstruction of the vertical velocity in the vertical
 187 advection term leads to a numerical error that is proportional to the horizontal divergence

$$188 \quad \mathcal{N}_d \sim \Delta^2 \int_0^z (\partial_x^2 d) dz \text{ in (1), and } \mathcal{N}_d \sim \Delta^2 \int_0^z (\partial_y^2 d) dz \text{ in (2).} \quad (9)$$

189 Here we have neglected the errors associated with the z -discretization since dispersive errors
 190 generated by the horizontal discretization are generally larger than vertical ones in typical
 191 ocean simulations where the grid cells are highly anisotropic.

192 We seek to improve the numerical error associated with vorticity reconstruction both by
 193 reducing its magnitude and also by computing the reconstruction so that the error is diffusive,
 194 and therefore “smooth”, rather than dispersive and “noisy”. For this we follow Ringler
 195 (2011), who proposed an upwind reconstruction of vorticity in the context of two-dimensional
 196 turbulence. Upwind reconstructions are diffusive: an upwind reconstruction of quantity a
 197 with respect to a velocity u leads to a truncation error that is proportional to $|u|\partial^n a$, with n
 198 an odd exponent equal to the upwinding order (Norman et al., 2023). The error of upwind
 199 vorticity reconstruction is proportional to an odd derivative of vorticity – hence an even
 200 derivative of the velocity field – and acts as a diffusion of momentum in the momentum
 201 equations:

$$202 \quad \mathcal{N}_\zeta \sim \Delta^n |v| \partial_y^n \zeta \text{ in (1), } \mathcal{N}_\zeta \sim \Delta^n |u| \partial_x^n \zeta \text{ in (2).} \quad (10)$$

203 This error will act diffusively also in the vorticity evolution equation as it is an even derivative
 204 of the vorticity, dissipating enstrophy in accordance with the forward enstrophy cascade
 205 characteristic of a two-dimensional flow.

206 Next, we turn to the vertical advection term. An upwind reconstruction of vertical
 207 advection in the rotational formulation is not achieved as easily as vorticity reconstruction or
 208 flux-form reconstruction (for example, as in Shchepetkin and McWilliams (1998b)), since the
 209 major source of dispersion is the advecting variable (w) rather than the vertical reconstruction
 210 of the advected quantity ($\partial_z u$). One of the major contributions of this work is to disentangle
 211 the dispersion related to the divergence field from a conservative vertical advection, by
 212 rewriting the vertical advection term using (3) such that

$$213 \quad D_t u = \underbrace{\partial_t u}_{\text{time derivative}} + \underbrace{\zeta v}_{\text{vorticity flux}} - \underbrace{u d}_{\text{divergence flux}} - \underbrace{\partial_z(wu)}_{\text{conservative vertical advection}} - \underbrace{\partial_x K}_{\text{kinetic energy gradient}}, \quad (11)$$

$$214 \quad D_t v = \underbrace{\partial_t v}_{\text{time derivative}} - \underbrace{\zeta u}_{\text{vorticity flux}} - \underbrace{v d}_{\text{divergence flux}} - \underbrace{\partial_z(wv)}_{\text{conservative vertical advection}} - \underbrace{\partial_y K}_{\text{kinetic energy gradient}}. \quad (12)$$

215 We have thus relegated the horizontal dispersive error, tied to the vertical velocity w , to a
 216 “divergence flux” term, akin to the vorticity flux. Contrary to the vertical advection terms
 217 in (1)–(2), the “divergence fluxes” in (11)–(12) are clearly amenable to an upwinding strategy.
 218 In particular, we use an upwind reconstruction of d with respect to u in ud term in (11),
 219 and vice versa an upwind reconstruction of d with respect to v in vd term in (12), which
 220 changes the dispersive error in (9) to

$$222 \quad \mathcal{N}_d \sim \Delta^n |u| \partial_x^n d \text{ in (1), and } \mathcal{N}_d \sim \Delta^n |v| \partial_y^n d \text{ in (2).} \quad (13)$$

223 Deriving the horizontal divergence evolution equation $\partial_x(1) + \partial_y(2)$ shows that this approach
 224 leads to a direct diffusion of the horizontal divergence. This implementation allows a
 225 mitigation of the dispersion inherent in the vertical velocity field as it removes spurious
 226 numerical divergent modes similar to how vorticity upwinding removes spurious numerical
 227 rotational modes.

228 2.2 Detailed implementation in the discrete primitive equations

229 We concretize the approach explained above on an orthogonal C-grid, where we define
 230 cell volumes \mathcal{V}_u , \mathcal{V}_v , \mathcal{V}_w , and \mathcal{V}_c for volumes at the u -, v -, w -velocity and tracer locations,
 231 respectively. The facial areas are denoted with \mathcal{A}_x , \mathcal{A}_y , and \mathcal{A}_z and the spacings with Δx ,
 232 Δy and Δz . As for volumes, we will use subscripts u , v , and w to denote the location of
 233 spacings Δx , Δy , and Δz . In addition to the angle bracket notations, we use double brackets
 234 and δ to express double-centered reconstructions and finite differences, respectively:

$$235 \quad \langle\langle a \rangle\rangle^{ij} \stackrel{\text{def}}{=} \left\langle \langle a \rangle^i \right\rangle^j, \quad \text{and} \quad \delta_i a \stackrel{\text{def}}{=} a_{i+1} - a_i. \quad (14)$$

236 Additionally, we use curly braces $\{\cdot\}$ to indicate upwinding where $\{a\}^i$ denotes an upwind
 237 reconstruction of variable a in the x -direction with respect to the x -velocity component (u).
 238 The specific formulation of the upwind reconstruction we use in this paper will be shown in
 239 section 3.

240 We indicate the discrete counterpart to the vorticity flux, the vertical advection, and
 241 the kinetic energy gradient, with \mathcal{Z} , \mathcal{V} , and \mathcal{K} , respectively. We use subscripts u and v
 242 to denote the x -momentum and y -momentum components of the discrete terms. As the
 243 material derivative of momentum (1)-(2) is discretized as follows:

$$244 \quad D_t u = \partial_t u + \mathcal{Z}_u - \mathcal{V}_u - \mathcal{K}_u, \quad (15)$$

$$245 \quad D_t v = \partial_t v - \mathcal{Z}_v - \mathcal{V}_v - \mathcal{K}_v, \quad (16)$$

247 We review here the centered-second order discretization schemes typically used in ocean
 248 modeling. The “energy conserving” centered second-order discretization of the vorticity flux
 249 term (Arakawa, 1966), later used as a reference, is

$$250 \quad \mathcal{Z}_u^E = \frac{\left\langle \langle \Delta x_v v \rangle^i \zeta \right\rangle^j}{\Delta x_u}, \quad \mathcal{Z}_v^E = \frac{\left\langle \langle \Delta y_u u \rangle^j \zeta \right\rangle^i}{\Delta y_v}. \quad (17)$$

251 The “enstrophy conserving” centered second-order discretization of the vorticity flux term
 252 (Arakawa, 1966) in this notation is

$$253 \quad \mathcal{Z}_u = \frac{\langle\langle \Delta x_v v \rangle\rangle^{ij}}{\Delta x_u} \langle \zeta \rangle^j, \quad \mathcal{Z}_v = \frac{\langle\langle \Delta y_u u \rangle\rangle^{ij}}{\Delta y_v} \langle \zeta \rangle^i. \quad (18)$$

254 \mathcal{K} is usually formulated as (Madec et al., 2022)

$$255 \quad \mathcal{K}_u = \frac{\langle \delta_i u^2 \rangle^i + \langle \delta_j v^2 \rangle^j}{2 \Delta x_u}, \quad \mathcal{K}_v = \frac{\langle \delta_j u^2 \rangle^i + \langle \delta_i v^2 \rangle^j}{2 \Delta y_v}, \quad (19)$$

256 while the discrete vertical advection \mathcal{V} is derived from \mathcal{K} to ensure the following integral
 257 energy conservation property (Madec et al., 2022):

$$258 \quad \sum_{i,j,k} (u \mathcal{V}_u \mathcal{V}_u + v \mathcal{V}_v \mathcal{V}_v) + \sum_{i,j,k} (u \mathcal{V}_u \mathcal{K}_u + v \mathcal{V}_v \mathcal{K}_v) = 0. \quad (20)$$

259 This property ensures that the change in discrete energy from the vertical advection term is
 260 balanced by the kinetic energy gradient. When paired with an energy-conserving vorticity flux
 261 implementation, the overall scheme conserves discrete energy in the system. The resulting
 262 formulation for \mathcal{V} is:

$$263 \quad \mathcal{V}_u = \frac{\left\langle \langle W \rangle^i \delta_k u \right\rangle^k}{\mathcal{V}_u}, \quad \mathcal{V}_v = \frac{\left\langle \langle W \rangle^j \delta_k v \right\rangle^k}{\mathcal{V}_v}. \quad (21)$$

264 The first step is to derive a suitable discrete form for the conservative vertical advection -
 265 divergence flux form of the material derivatives (11)-(12). We denote with \mathcal{C} and \mathcal{D} the

discrete counterpart to the conservative vertical advection and the divergence flux. To derive suitable candidates for \mathcal{C} and \mathcal{D} , we manipulate \mathcal{V} to ensure discrete energy conservation through

$$\sum_{i,j,k} (u \mathcal{V}_u \mathcal{V}_u + v \mathcal{V}_v \mathcal{V}_v) = \sum_{i,j,k} [u \mathcal{V}_u (\mathcal{C}_u + \mathcal{D}_u) + v \mathcal{V}_v (\mathcal{C}_v + \mathcal{D}_v)]. \quad (22)$$

The derivation is performed in [Appendix B](#) (note that $\mathcal{V} \neq \mathcal{C} + \mathcal{D}$ locally). The resulting discrete formulations read

$$\mathcal{C}_u = \frac{\delta_k (\langle W \rangle^i \langle u \rangle^k)}{\mathcal{V}_u}, \quad \mathcal{C}_v = \frac{\delta_k (\langle W \rangle^j \langle v \rangle^k)}{\mathcal{V}_v}, \quad (23)$$

$$\mathcal{D}_u = \frac{u \langle D \rangle^i}{\mathcal{V}_u}, \quad \mathcal{D}_v = \frac{v \langle D \rangle^j}{\mathcal{V}_v}, \quad (24)$$

where $D = \delta_i U + \delta_j V$ is the discrete horizontal divergence, $U = \mathcal{A}_x u$, $V = \mathcal{A}_y v$, and $W = \mathcal{A}_z w$. With a formulation for \mathcal{C} and \mathcal{D} , we have found a suitable, energy-conserving discretization of equations [\(11\)-\(12\)](#):

$$D_t u = \partial_t u + \mathcal{Z}_u - \mathcal{D}_u - \mathcal{C}_u - \mathcal{K}_u, \quad (25)$$

$$D_t v = \partial_t v - \mathcal{Z}_v - \mathcal{D}_v - \mathcal{C}_v - \mathcal{K}_v. \quad (26)$$

281

The second step consists in correctly upwinding fluxed variables. Following our approach, we implement an upwind reconstruction of vorticity in [\(18\)](#) by substituting the following terms

$$\langle \zeta \rangle^i \mapsto \{\zeta\}^i \text{ and } \langle \zeta \rangle^j \mapsto \{\zeta\}^j. \quad (27)$$

The same can be done for \mathcal{C} and \mathcal{D} , where an upwind reconstruction is ensured by

$$\langle u \rangle^k \mapsto \{u\}^k \text{ and } \langle v \rangle^k \mapsto \{v\}^k, \quad (28)$$

$$\langle D \rangle^i \mapsto \{D\}^i \text{ and } \langle D \rangle^j \mapsto \{D\}^j. \quad (29)$$

As we show in [Appendix C](#), numerical errors that scale with a cross-derivative of the velocity field can lead to grid-scale energy generation instead of energy dissipation. For example, since $d = \partial_x u + \partial_y v$, a straightforward first-order upwind reconstruction of d in the x -direction leads to

$$\mathcal{N}_d \sim |u|(\partial_x^2 u + \partial_x \partial_y v), \quad (30)$$

where $\partial_x^2 u$ is diffusive while $\partial_x \partial_y v$ has the potential to be anti-diffusive. The opposite happens in the y -direction. To avoid injecting energy at the grid scale, we define the upwind reconstruction of the discrete divergence as a reconstruction that guarantees discrete energy dissipation. For this reason, we implement upwinding of D as follows

$$\{D\}^i \stackrel{\text{def}}{=} \{\delta_i U\}^i + \langle \delta_j V \rangle^i, \quad (31)$$

$$\{D\}^j \stackrel{\text{def}}{=} \langle \delta_i U \rangle^j + \{\delta_j V\}^j. \quad (32)$$

We follow the same implementation for \mathcal{K} , where we recognize the similarity between \mathcal{D} and \mathcal{K} ($u \partial_x u = \frac{1}{2} \partial_x u^2$ and $v \partial_y v = \frac{1}{2} \partial_y v^2$) and can safely substitute

$$\langle \delta_i u^2 \rangle^i \mapsto \{\delta_i u^2\}^i \text{ and } \langle \delta_j v^2 \rangle^j \mapsto \{\delta_j v^2\}^j, \quad (33)$$

in equation [\(19\)](#).

The approach we sketched results in a method that is energetically dissipative, tackles stability issues through an upwinding strategy, and removes grid-scale variance when applied to the rotational form of the primitive equations. The main ingredients are the splitting of the vertical advection term [\(11\)-\(12\)](#), the discrete energy conserving implementation [\(23\)-\(24\)](#)

310 followed by the targeted upwind substitutions (27), (28), (29), and (33). We have not yet
 311 described how to perform the upwinding, which, in principle, can be done with any diffusive
 312 reconstruction scheme. In the next section, we propose a WENO-based reconstruction that
 313 pairs with the discretization detailed above by allowing a notably lower level of energy
 314 dissipation compared to other upwinding strategies.

315 3 WENO reconstruction scheme for the rotational primitive equations

316 The Weighted Essentially Non-Oscillatory (WENO) scheme is a particular implemen-
 317 tation of the Essentially Non-Oscillatory schemes first introduced by [Harten et al. \(1987\)](#)
 318 and refined by [Shu \(1997\)](#). The WENO scheme is especially appropriate to resolve shocks
 319 that develop in solutions of partial differential equations such as the Euler equations or
 320 the shallow water equations. The central idea behind the WENO scheme is to dynamically
 321 approximate a numerical flux with multiple low-order reconstructing polynomials. These
 322 polynomials are combined using nonlinear weights that depend on the smoothness of each
 323 individual polynomial, with the objective of obtaining a high-order upwind reconstruction
 324 in smooth regions and lower-order upwind reconstruction in regions where the solution is
 325 less smooth. This approach allows the scheme to achieve high accuracy even in regions of
 326 high gradients and discontinuities while, at the same time, avoiding artificial oscillations
 327 (dispersive artifacts) that plague conventional high-order methods.

328 We start by reviewing the mathematical implementation of a WENO reconstruction.
 329 Given a discrete quantity ϕ , we denote with $[\phi]_r^i$ the one-dimensional reconstruction obtained
 330 by the r -th candidate polynomial of order s ($p_{r\phi}$ for $r \in \{0, \dots, s-1\}$) in the i -th direction,
 331 that is:

$$332 [\phi]_r^i \stackrel{\text{def}}{=} p_{r\phi}(x_{i+1/2}) = \sum_{j=0}^{s-1} c_{rj} \phi_{i-r+j}, \quad \text{with } r \in \{0, \dots, s-1\}. \quad (34)$$

333 where ϕ_{i-r+j} is the average ϕ in cell $i-r+j$, c_{rj} are linear reconstructing weights and $x_{i+1/2}$
 334 is the final x position of $[\phi]_r^i$ on the discrete grid ([Shu, 1997](#)). The WENO reconstruction
 335 procedure is a convex combination of the candidate reconstructions and is implemented as
 336 follows:

$$337 \{\phi\}^i = \sum_{r=0}^{s-1} \xi_{r\phi} [\phi]_r^i, \quad \text{with } \xi_{r\phi} = \frac{\alpha_{r\phi}}{\sum_{r=0}^{s-1} \alpha_{r\phi}} \text{ and } \alpha_{r\phi} = f(\alpha_r^*, \beta_{r\phi}). \quad (35)$$

338 Above, ξ_r are the nonlinear WENO weights, which are functions of the optimal linear
 339 weights (α_r^*) weighted by a measure of smoothness of the field $\beta_{r\phi}$, where the subscript ϕ
 340 indicates that β is calculated from field ϕ . The α_r^* optimal linear weights are obtained by
 341 equating the final reconstruction $\{\phi\}^i$ to a classical upwind biased reconstruction of order
 342 $2s-1$ when the field ϕ is smooth ($\beta_{r\phi} = 0$ for each $r \in \{0, \dots, s-1\}$). Several formulations
 343 for smoothness weighting (f) have been put forth, and, while the exact formulation of the α
 344 weights is not a central concern of this work, it is noteworthy to mention that we employ the
 345 WENO-Z formulation ([Balsara & Shu, 2000](#)). In terms of smoothness indicators, the most
 346 widespread approach is to use a Sobolev norm of the reconstructing polynomial $p_{r\phi}$ over the
 347 interval $(x_{i-1/2}, x_{i+1/2})$ ([Shu, 1997](#)):

$$348 \beta_{r\phi} \stackrel{\text{def}}{=} \sum_{\ell=1}^{s-1} \int_{x_{i-1/2}}^{x_{i+1/2}} \Delta x^{2\ell-1} (\partial_x^\ell p_{r\phi})^2 dx. \quad (36)$$

349 For “flux-form” advection, the reconstructed field is typically the same as the field that
 350 is advanced in time. As such, using ϕ to compute β_r , directly connects the smoothness
 351 evaluation to the evolved quantity. This is not the case in the rotational form of the
 352 Navier–Stokes equations where the field evolved in time is typically not the same as the field
 353 being reconstructed. Specifically, in the derivation outlined in the preceding section, upwind

354 reconstruction is applied to six distinct quantities:

355 $\{\zeta\}^j, \{u\}^k, \{D\}^i, \{\delta_i u^2\}^i$ in the u evolution equation, (37)

356 $\{\zeta\}^i, \{v\}^k, \{D\}^j, \{\delta_j v^2\}^j$ in the v evolution equation. (38)

358 Many terms in (37)-(38) above involve derivatives of the velocities and thus exhibit
 359 rapid variations at the grid scale compared to the dynamics of the horizontal momentum
 360 fields. In this context, we found that $\beta_{r\phi}$ is an inadequate smoothness measure since it lacks
 361 an intuitive connection with the dynamics of the evolved field – specifically, the velocity
 362 field, which is significantly smoother than the upwinded quantities. Due to this discrepancy,
 363 $\beta_{r\phi}$ in (35) causes an artificial decrease of the WENO reconstruction order leading to a
 364 larger-than-necessary dissipation. We demonstrate this in section 4 within the context of two-
 365 dimensional decaying turbulence and in section 5 within the context of a three-dimensional
 366 baroclinic jet.

367 Based on the above discussion, we propose here an alternative approach to assess
 368 smoothness, wherein we employ the reconstructing polynomials of a “parent” (smoother)
 369 field constructed directly from velocities, rather than from their derivatives. An exception is
 370 the divergence flux: we find that the divergence flux term contributes the most to grid-scale
 371 noise and, as such, we choose to diffuse it consistently with its intrinsic smoothness. We
 372 introduce notation to facilitate the description and understanding of our approach. In this
 373 notation, a WENO reconstruction is denoted as

374 $\{\phi; \psi\},$ (39)

375 where ϕ represents the field being reconstructed and ψ is the field used for assessing the
 376 smoothness. We use the notation $\{\phi; \psi\}^i$ as short-hand for the following reconstruction

377 $\{\phi; \psi\}^i = \sum_{r=0}^{s-1} \xi_{r\psi} [\phi]_r^i,$ (40)

378 where $\xi_{r\psi}$ is calculated using (35)-(36) and $p_{r\psi}$ (the reconstructing polynomials of quantity ψ).
 379 Under the conventional WENO scheme, where the reconstructed and smoothness-diagnosed
 380 fields are identical, this notation simplifies to $\{\phi; \phi\}$. Where not explicitly stated, $\{\phi\}$ denotes
 381 a WENO reconstruction with standard smoothness stencils, that is $\{\phi\} = \{\phi; \phi\}$.

382 The smoothness-optimized upwind WENO reconstructions, written in the above-
 383 presented notation, are

384 $\{\zeta; \mathbf{u}\}^j, \{u\}^k, \{D; D\}^i, \{\delta_i u^2; \langle u \rangle^i\}^i$ in the u evolution equation, (41)

385 $\{\zeta; \mathbf{u}\}^i, \{v\}^k, \{D; D\}^j, \{\delta_j v^2; \langle v \rangle^j\}^j$ in the v evolution equation, (42)

387 where we define the upwinding of ζ as an average between a u -based and a v -based recon-
 388 struction:

389
$$\{\zeta; \mathbf{u}\} \stackrel{\text{def}}{=} \frac{\{\zeta; \langle u \rangle^j\} + \{\zeta; \langle v \rangle^i\}}{2}.$$
 (43)

Using reconstructed variables $\langle v \rangle$ and $\langle u \rangle$ as smoothness metrics and not u and v directly is
 a consequence of the staggered C-grid discretization. Note the difference between $\{D\}$ and
 $\{D; D\}$: while the first uses the individual velocity derivatives as a smoothness measure, the
 second uses the whole discrete divergence:

390 $\{D\}^i = \{\delta_i U; \delta_i U\}^i + \{\delta_j V\}^i, \quad \{D\}^j = \{\delta_i U\}^j + \{\delta_j V; \delta_j V\}^j,$ (44)

391 $\{D; D\}^i = \{\delta_i U; D\}^i + \{\delta_j V\}^i, \quad \{D; D\}^j = \{\delta_i U\}^j + \{\delta_j V; D\}^j.$ (45)

This difference has a large impact on the solution as, usually, $\delta_j V$ and $\delta_i U$ have a cancellation
 effect.

Table 1. Description of test cases

Name	Legend	Vorticity Flux	Vorticity smoothness	SGS closure
DNS	—	Energy conserving	—	—
Leith1	---	Energy conserving	—	Leith, $\mathbb{C} = 1$
Leith2	—	Energy conserving	—	Leith, $\mathbb{C} = 2$
W5D	---	WENO 5th order	$\{\zeta\}$	—
W9D	—	WENO 9th order	$\{\zeta\}$	—
W5V	---	WENO 5th order	$\{\zeta; \mathbf{u}\}$	—
W9V	—	WENO 9th order	$\{\zeta; \mathbf{u}\}$	—

4 Two-dimensional homogeneous decaying turbulence test case

We begin by evaluating our novel momentum advection scheme using simulations of decaying two-dimensional homogeneous turbulence. The purpose of this test is to compare our momentum advection scheme with dispersive numerics in a setting where it is computationally feasible to run Direct Numerical Simulations (DNS), i.e. simulations that resolve scales down to the physical dissipation. The DNS serves as the benchmark, allowing us to assess the performance of the different approaches at coarser resolutions. To further investigate the impact of decoupling the reconstruction polynomials from the smoothness assessment, we examine the reconstruction of vorticity using both $\{\zeta; \mathbf{u}\}$ and $\{\zeta\}$. This test case is well-suited to assess the discrete properties of the vorticity flux reconstruction, because there are no divergent motions in two dimensions.

We solve the incompressible two-dimensional Navier–Stokes equations in non-dimensional form, i.e.,

$$\partial_t \mathbf{u} + \zeta \hat{\mathbf{k}} \times \mathbf{u} = -\nabla(p + K) + \frac{1}{Re} \nabla^2 \mathbf{u} + \nabla \cdot \boldsymbol{\tau}_{SGS}, \quad (46)$$

$$\nabla \cdot \mathbf{u} = 0. \quad (47)$$

Notice that \mathbf{u} and ∇ denote the two-dimensional rather than the three-dimensional velocity vector and gradient in this section. The simulations are run with a $Re = 3.3 \times 10^4$ on a doubly periodic box of nondimensional size $2\pi \times 2\pi$. The equations are evolved using a low-storage third-order Runge–Kutta scheme and a pressure projection method that utilizes an FFT elliptical solver.

We initialize the simulations with velocities generated through a narrow-band energy spectrum as proposed by Ishiko et al. (2009),

$$E(k) = \frac{1}{2} a_s k_p^{-1} \left(\frac{k}{k_p} \right)^7 \exp \left[-\frac{7}{2} \left(\frac{k}{k_p} \right)^2 \right], \quad (48)$$

where $k \stackrel{\text{def}}{=} (k_x^2 + k_y^2)^{1/2}$ is the magnitude of the wavenumber vector, $a_s = 16/3$, and $k_p = 12$ is the wavenumber corresponding to maximum energy. With this choice of initial condition and Reynolds number, we achieve a good spectral separation between the energy-containing and dissipation scales. To construct a velocity field with this energy spectrum, we first generate a vorticity field in Fourier space

$$\hat{\zeta}(k_x, k_y) = \left[\frac{k}{\pi} E(k) \right]^{1/2} e^{i\phi(k_x, k_y)}, \quad (49)$$

where $\phi(k_x, k_y)$ are random phases chosen such that the vorticity field in physical space is real (Ishiko et al., 2009). The initial velocity distributions are then given by:

$$\hat{u}(k_x, k_y) = \frac{ik_y}{k^2} \hat{\zeta}(k_x, k_y), \quad \hat{v}(k_x, k_y) = -\frac{ik_x}{k^2} \hat{\zeta}(k_x, k_y). \quad (50)$$

The simulations are run for $t = 6$ nondimensional time units.

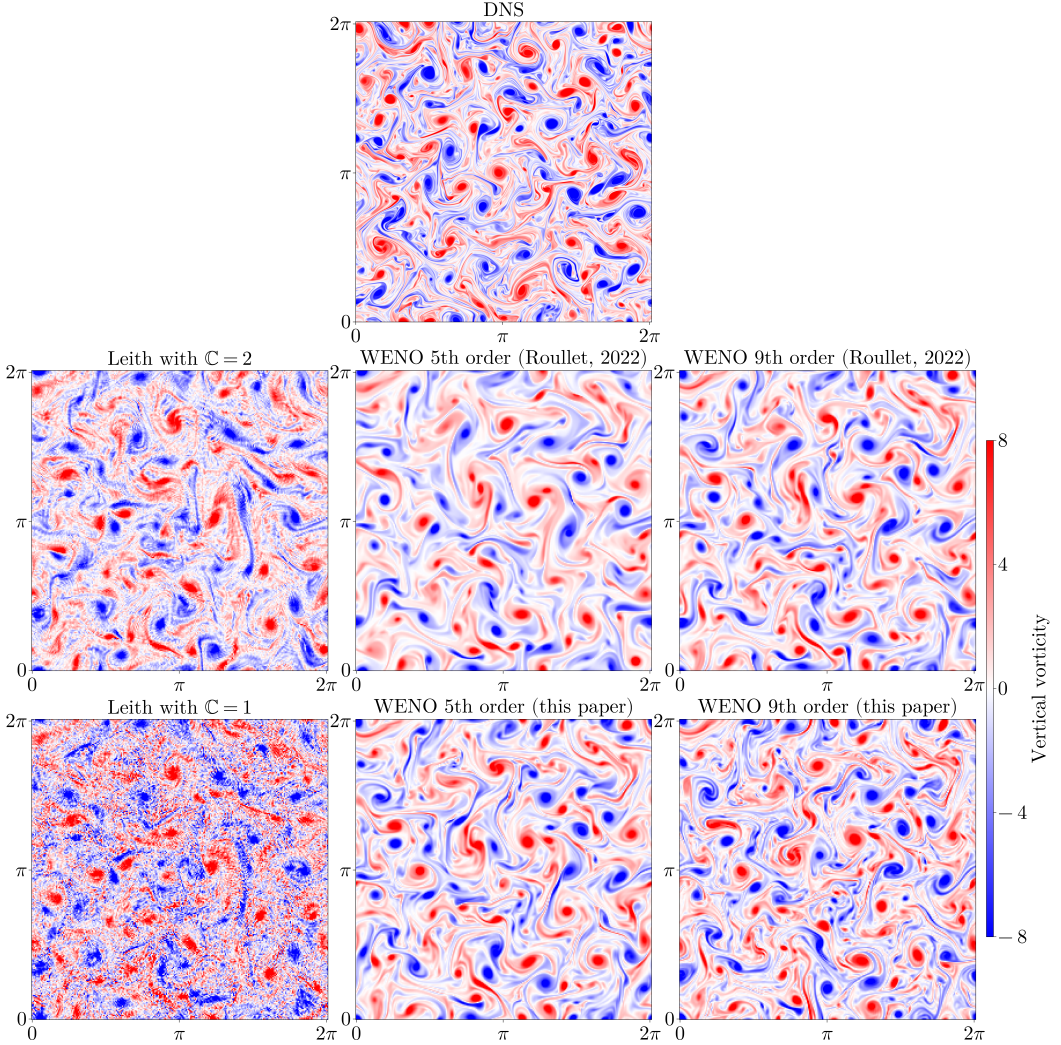


Figure 3. Vorticity at $t = 3.6$ after initialization. Comparison between DNS (top panel), explicit LES with a Leith viscosity (left panels), and implicit LES with a rotational WENO discretization with $N = 256^2$. Of the WENO schemes, the top panels show the results obtained with a standard WENO reconstruction of vorticity $\{\zeta; \zeta\}$ (W5D and W9D in table 1) while the bottom panels show a reconstruction using the velocity field as smoothness measure $\{\zeta; \mathbf{u}\}$ (W5V and W9V in table 1).

The fully resolved benchmark solution employs the second-order energy-conserving advection discretization, as per eq. (17) and $N = 4096 \times 4096$ grid points. We compare it with solutions obtained using coarser grids and three distinct methods. The first is a second-order energy-conserving advection operator stabilized by the Leith closure (see Appendix A). We do not consider the adaptive Leith scheme, because it is too expensive for oceanographic applications. Instead, we consider the traditional Leith scheme for two different values of the nondimensional parameter C : $C = 1$ and $C = 2$. The second method involves the rotational WENO, using standard smoothness diagnosis $\{\zeta\}$ as in the work by Roulet and Gaillard (2022). The third method employs the new rotational WENO, where vorticity is reconstructed as $\{\zeta; \mathbf{u}\}$. For the WENO schemes, we compare fifth- and ninth-order reconstruction. All the different methods are summarized in table 1.

The grid size for the under-resolved simulations is ramped up from 64×64 , where only the largest structures are resolved, to 128×128 , 256×256 , and finally 1024×1024 , where the grid is fine enough to resolve most of the energy and enstrophy spectra. For reference, in

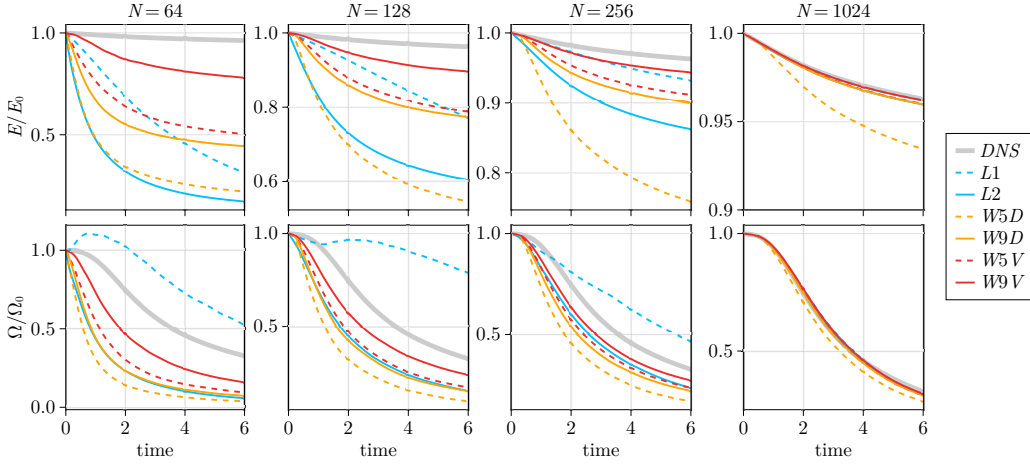


Figure 4. Evolution in time of integrated kinetic energy (top row) and integrated enstrophy (bottom row). Advection schemes and numerical details are shown in table 1.

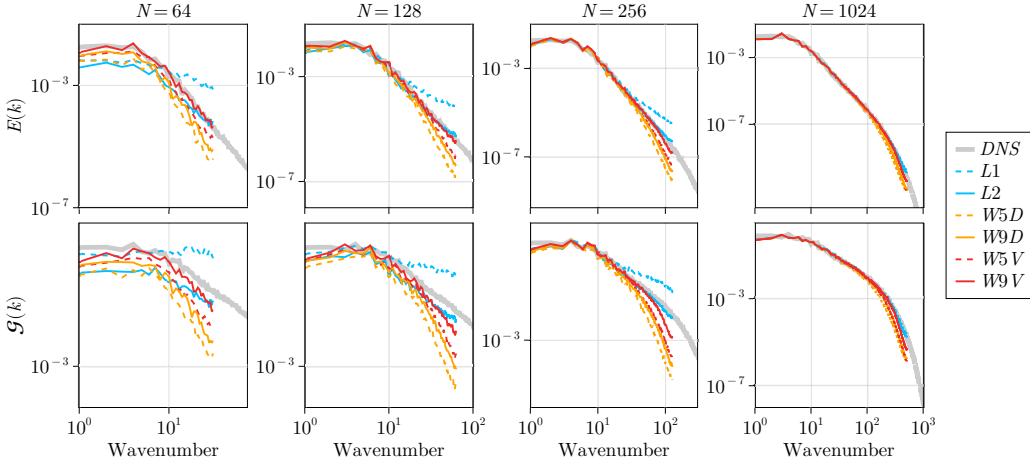


Figure 5. Kinetic energy spectra (top panels) and enstrophy spectra (bottom panels) at $t = 3.6$. Advection schemes and numerical details are shown in table 1.

a high-resolution global ocean simulation, the grid barely resolves the largest-scale eddies and is therefore more similar to the 64×64 or 128×128 case than the 1024×1024 .

Figure 3 shows a comparison of the vertical vorticity at $t = 3.6$. The top panel shows the DNS solution, while the center and bottom panels show the under-resolved simulations. The Leith closure, even when using the larger parameter $C = 2$, results in substantial nonphysical noise at the grid scale. In contrast, all WENO-based reconstructions yield a turbulent solution completely devoid of grid-scale noise. The dynamics at small scales is better resolved with higher WENO order as evidenced by the appearance of well resolved structures close to the grid-scale. The same result can be noticed when switching from standard WENO smoothness stencils to $\{\zeta; \mathbf{u}\}$.

Figure 4 illustrates the evolution of kinetic energy (top panels) and enstrophy (bottom panels) for the various methods at different resolutions. The evolution of both quantities converges to the DNS solution at 1024×1024 for all methods as the resolution is increased, except for the WENO fifth-order with standard vorticity reconstruction (W5D) which exhibits excessive energy dissipation. As for the Leith closures, they do converge to the DNS solution

455 at the highest resolution (1024×1024) but are severely deficient at coarser resolutions. With
 456 $C = 1$, the solutions have too large enstrophy as the closure fails to remove grid-scale vorticity
 457 stemming from the centered advection scheme. With $C = 2$ the enstrophy levels are reduced,
 458 but at the cost of too low kinetic energy. The difference between $C = 1$ and $C = 2$ illustrates
 459 the fundamental challenge with using dispersive numerical methods: removing spurious
 460 dispersive artifacts can require excessively high dissipation with the unintended consequence
 461 of reducing the large scale energy in the system. Conversely, the WENO reconstruction
 462 schemes are designed to limit dispersive artifacts while maintaining high-order reconstruction
 463 that retains large-scale energy. Figure 4 shows that, as expected, the accuracy of the WENO
 464 approach increases with a higher discretization order. Most importantly the smoothness
 465 measure obtained with the new stencils $\{\zeta; \mathbf{u}\}$ achieves a higher effective resolution, i.e.
 466 converges faster to the DNS solution.

467 Figure 5 shows the energy (top panels) and enstrophy (bottom panels) spectra at $t = 3.6$.
 468 Again, all methods converge to the DNS solution at 1024×1024 (in the inertial range),
 469 except for the W5D case. At lower resolutions, the Leith closure with $C = 1$ fails to match
 470 the DNS spectra and exhibits a pile-up of variance at small scales. Using a larger parameter
 471 ($C = 2$) reduces the bias in small-scale variance at the expense of excessive damping of energy,
 472 especially at large scales; this is hard to appreciate in Fig. 5 because of the logarithmic scale,
 473 but is clear in Fig. 4. WENO reconstructions do overly dissipate enstrophy at small scales,
 474 as they are designed to do, but the energy spectra are much better captured especially with
 475 the $\{\zeta; \mathbf{u}\}$ reconstruction. This is vindication that the upwinding of vorticity dissipates
 476 enstrophy, but not energy, at small scales. In this case, a ninth-order WENO reconstruction
 477 of vorticity, using $\{\zeta; \mathbf{u}\}$ stencils (W9V), captures the DNS energy spectrum at all resolutions,
 478 down to 64×64 .

479 In conclusion, in the context of two-dimensional decaying turbulence, the explicit Leith
 480 closure accurately represents the DNS solution only at the highest resolution but fails at
 481 lower resolutions. This failure stems from the oscillatory dynamics of the centered advection
 482 scheme that produce grid-scale noise which is not selectively damped by the Leith closure.
 483 In practice, the closure results in either too much enstrophy at small scales or too little
 484 energy at all scales depending on parameter choices. In contrast, a WENO reconstruction
 485 of vorticity using $\{\zeta; \mathbf{u}\}$ dissipates enstrophy at small scales and preserves an accurate
 486 energy spectrum at all scales. Additionally, this test case demonstrates the benefit of using
 487 high-order reconstruction stencils, as the ninth-order scheme produces a much more energetic
 488 solution that converges to DNS at coarser resolution compared to the fifth-order counterpart.
 489 We conclude that, for this case, the W9V approach comes closer to achieving the LES goal
 490 of resolution independence than the other methods explored in this section.

491 5 Baroclinic jet test case

492 Next, we test our rotational WENO reconstruction in a baroclinic jet setup. The setup
 493 consists of a periodic channel in a spherical sector between $60^\circ\text{S} - 40^\circ\text{S}$, 20 degrees wide, and
 494 one kilometer deep. The simulations are initialized with a constant vertical stratification
 495 $N^2 = 4 \times 10^{-6} \text{ s}^{-2}$ and a meridional buoyancy front given by:

$$496 b(\phi, z) = N^2 z + \Delta b \begin{cases} 0 & \text{if } \gamma(\phi) < 0 , \\ [\gamma(\phi) - \sin \gamma(\phi) \cos \gamma(\phi)]/\pi & \text{if } 0 \leq \gamma(\phi) \leq \pi , \\ 1 & \text{if } \pi < \gamma(\phi) , \end{cases} \quad (51)$$

$$497 498 \gamma(\phi) = \frac{\pi}{2} - 2\pi \frac{\phi - \phi_0}{\Delta\phi} , \quad (52)$$

499 where $\phi_0 = 50^\circ\text{S}$ is the central latitude of the domain, $\Delta\phi = 20^\circ$ the domain's latitudinal
 500 extent, $\Delta b = 5 \times 10^{-3} \text{ m s}^{-2}$. The initial velocity is in thermal-wind balance with the
 501 buoyancy field and vanishes at $z = -H$. Thus the initial conditions are an equilibrium

Table 2. Details of the different advection schemes used.

Method Name	Dispersive	Upwind	WENO
Rotational form \mathcal{Z}	Energy conserving (17)	—	WENO 9th-order
Rotational form \mathcal{V}	Centered 2nd-order (21)	—	—
Rotational form \mathcal{D}	—	—	WENO 9th-order
Rotational form \mathcal{C}	—	—	WENO 5th-order
Rotational form \mathcal{K}	Centered 2nd order (19)	—	WENO 5th-order
Flux-form advection	—	Upwind 3rd-order	—
Tracer advection	WENO 7th-order	WENO 7th-order	WENO 7th-order

Table 3. Computational details of the test cases. The advection column refers to the details shown in table 2. Each case consists of three simulations with a horizontal resolution of 1/8th, 16th, and 1/32nd of a degree.

	Advection	Smoothness	explicit closure
UP3	Upwind	—	—
W9V	WENO	Eqs. (41) and (42)	—
W9D	WENO	Eqs. (37) and (38)	—
SM2	Dispersive	—	Smagorinsky (Appendix A)
QG2	Dispersive	—	QG Leith with $C = 2$ (Appendix A)

solution to the primitive equations, but one that is unstable to the development of baroclinic instability (Vallis, 2017).

The initial buoyancy and velocity profiles are shown in figure 6. We add a weak white noise to the profile to kick-start the baroclinic instability (not shown in the figure). We impose no-flux and free-slip boundary conditions on all solid walls. We also prescribe a background vertical viscosity $\nu = 10^{-4} \text{ m}^2 \text{ s}^{-1}$ and a vertical diffusivity $\kappa = 10^{-5} \text{ m}^2 \text{ s}^{-1}$. To sustain turbulence and allow an equilibrated solution, we linearly restore the zonally averaged buoyancy and velocity to the initial profiles with a timescale of 50 days (in a similar manner as done by Soufflet et al. (2016)). This restoring sets the zonal transport without interfering with the development of mesoscale eddies, which are the focus of this test. We run the simulations for a total of 1000 days.

We conduct a series of simulations using different momentum advection approaches. Three dispersive schemes: (1) our novel advection scheme (W9V) with ninth-order WENO reconstruction of vorticity (\mathcal{Z}) and divergence (\mathcal{D}), and a 5th order for \mathcal{C} , and \mathcal{K} as their order has minimal impact on the solution; (2) a WENO reconstruction of the same order with standard smoothness stencils (W9D) for both vorticity flux $\{\zeta\}$, divergence flux $\{D\}$, and kinetic energy gradient $\{\delta \cdot \mathbf{u}^2\}$; (3) a third-order flux-form upwind-biased advection (UP3), commonly used in regional ocean modeling (Shchepetkin & McWilliams, 1998b; Madec et al., 2022).

Dispersive schemes are unstable without lateral diffusion, therefore, to benchmark against dispersive schemes, we consider a second-order energy-conserving discretization of the momentum advection term in the rotational form, stabilized by two different explicit closures: (1) a lateral friction closure composed by a laplacian and a bilaplacian combination of a static viscosity and a Smagorinsky-type eddy viscosity (SM2) described in Appendix A (Smagorinsky, 1963); (4) a quasi-geostrophic counterpart to the two-dimensional Leith closure, with $C = 2$ (QG2), designed to satisfy the forward cascade of potential vorticity (Bachman et al., 2017). The details of these explicit closures are summarized in Appendix A.

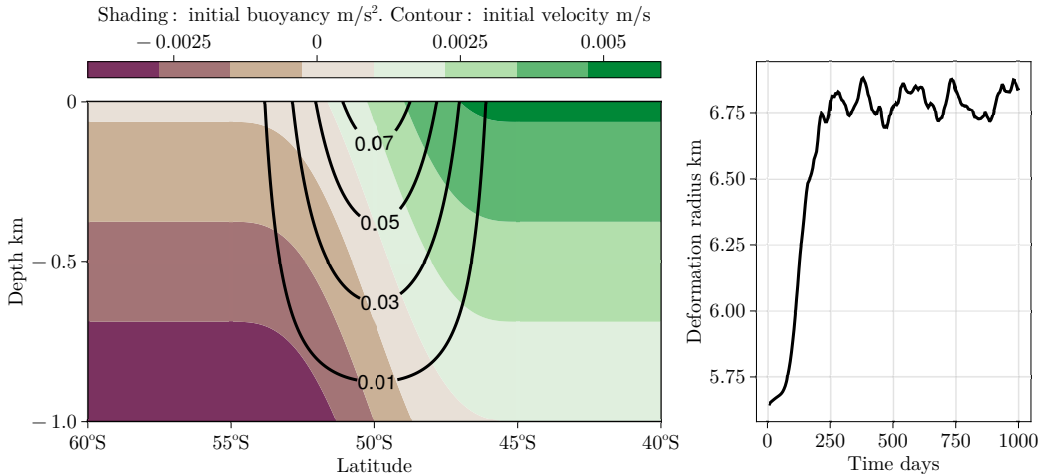


Figure 6. Left: The initial conditions (51): buoyancy (shading) and zonal velocity (contours). Right: The evolution of the domain-average deformation radius for the W9V case at 7km resolution.

These explicit closures are not chosen because we believe that they are best in class, but rather because most OGMs use either a Smagorinsky closure, a Leith closure, a constant viscosity, or a combination of the three. Additional information about the test cases is given in tables 2 and 3.

Tracer advection is more expensive than rotational-form momentum advection given the three-dimensional nature of the scheme when compared to the two-dimensional vorticity flux. We find that a 7th-order tracer advection scheme is a good compromise between efficiency and accuracy, and for this reason, we use a 7th-order WENO scheme for buoyancy advection in all test cases. Each set consists of three simulations run with horizontal resolutions of 1/8th, 1/16th, and 1/32nd of a degree, equivalent to a maximum (meridional) grid spacing of 14 km, 7 km, and 3.5 km, respectively. The vertical grid spacing is fixed at 20 meters. The equations are evolved in time using a second-order Adams-Bashforth scheme and a subcycling scheme for the two-dimensional free surface.

The jet undergoes an initial baroclinic instability that develops into a statistically steady state around the 250th day, when the eddy kinetic energy dissipation balances the injection of potential energy generated by the buoyancy restoring. The most unstable mode of a baroclinically unstable jet is close to the deformation radius defined as (Vallis, 2017):

$$L_d \stackrel{\text{def}}{=} \frac{1}{\pi|f|} \int_{-H}^0 (\partial_z b)^{1/2} dz. \quad (53)$$

A fully resolved simulation requires a horizontal spacing finer than L_d . How much finer depends on the numerical scheme: given the vigorous inverse energy cascade characteristic of quasi-geostrophic turbulence, a lower dissipation results in convergence at a coarser resolution. An eddy-permitting simulation has a grid size of the same order as the deformation radius (10-50 km in the ocean). In this baroclinic jet setup, the initial deformation radius is 5.5 km and adjusts to an equilibrium value of about 6.75 km as shown in figure 6. Thus, the highest resolution simulations are barely “resolved” with slightly more than one grid cell per deformation radius, while the 14 km tests are “under-resolved”. The 7-kilometer simulations are in a dynamical regime representative of typical eddy-permitting ocean models, which are run with a horizontal spacing between 10-20 km.

Figure 7 shows surface vorticity at different resolutions at the end of the initial transient (day 220). The panels are organized by increasing resolution from top to bottom and increasing kinetic energy from left to right (except the leftmost panels which show the W9V solution). As resolution increases, eddy activity spreads to higher and lower latitudes,

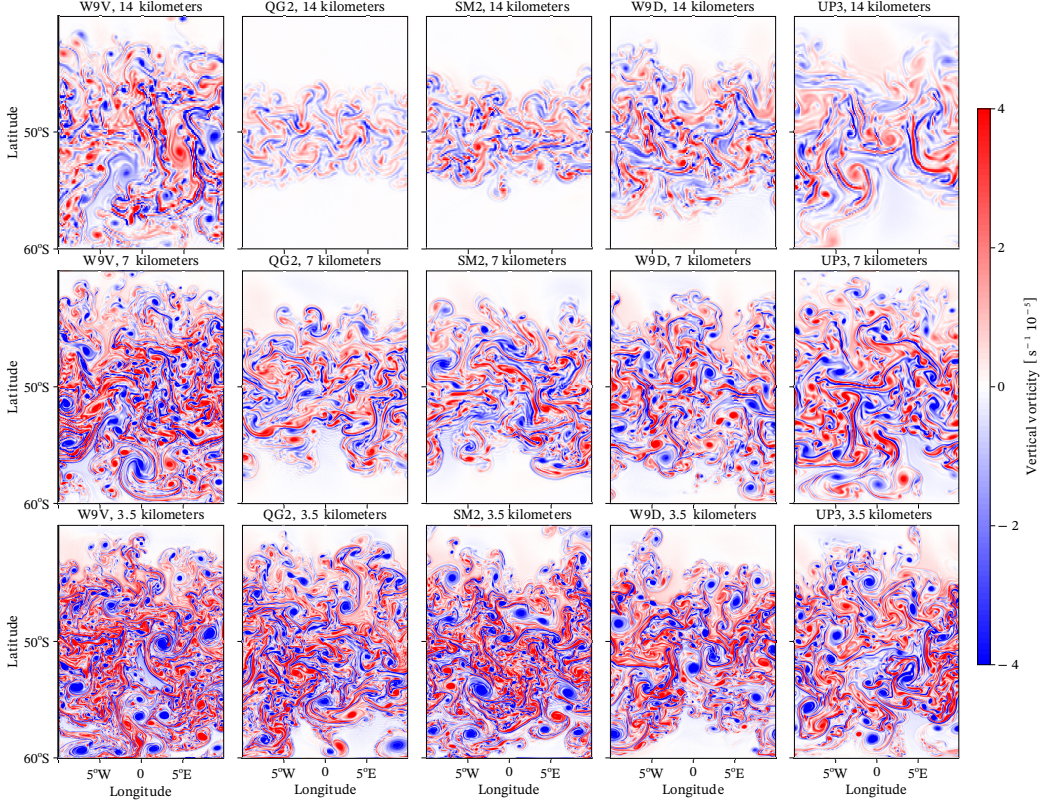


Figure 7. Near-surface vorticity at 14 (top panels), 7 (center panels), and 3.5-kilometer (bottom panels) resolution during the initial instability phase (day 230). The leftmost panel shows W9V while the remaining panels (from left to right) are ordered by increasing kinetic energy.

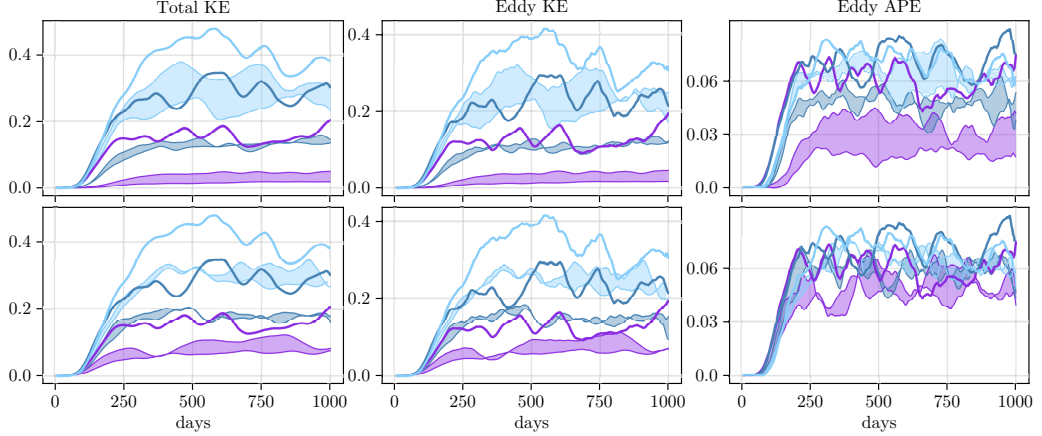


Figure 8. 10-day running average of integrated total kinetic energy, eddy kinetic energy, and eddy available potential energy. The solid lines are W9V at 14 km (blue), 7 km (steel blue), and 3.5 km resolution (light blue). The banded lines of the same colors show the maximum and minimum trajectory for the dispersive cases (top: SM2, QG2) and diffusive schemes (bottom: UP3, W9D).

561 indicating that the frontal slumping has extended further in the domain. Interestingly, W9V
 562 shows a large spread of vorticity even in the 14 km case where the deformation radius is
 563 severely under-resolved. The dispersive cases show evidence of spectral ringing at 7 and
 564 3.5 km resolutions.

565 The time series of total kinetic energy, eddy kinetic energy, and eddy potential energy
 566 are shown in Figure 8. In the top panels, W9V is compared to the dispersive approaches
 567 (SM2, and QG2), while in the bottom panels W9V is compared to the diffusive schemes
 568 (UP3 and W9D). As expected, increasing resolution results in more APE to EKE conversion.
 569 The length of the initial transient until the solution becomes fully turbulent decreases with
 570 increasing resolution until it converges at 7 km for W9V, and at 3.5 km for all the other
 571 cases. We attribute this difference to the fact that all explicit closures assume fully turbulent
 572 flow, whereas during the initial condition the growth of baroclinic instability is laminar. The
 573 amount of implicit dissipation with W9V, instead, is proportional to the smoothness of the
 574 resolved flow and thus smaller during the laminar phase as it should be. The panels in
 575 Figure 8 show that solutions using W9V converge at half the resolution (or more) during the
 576 initial instability growth.

577 The transformation of mean APE to EKE occurs through generation of eddy APE by
 578 baroclinic instability of the mean flow. The eddy APE is then converted to EKE through the
 579 vertical eddy flux ($w'b'$). Eddy available potential energy and eddy kinetic energy are further
 580 removed from the system by dissipation and by the restoring to thermal wind balance. The
 581 much larger EKE in the W9V cases when compared to the other test cases suggests that
 582 the implicit dissipation intrinsic in the W9V scheme is significantly lower than the (explicit)
 583 energy dissipation provided by the explicit closures and the (implicit) dissipation provided
 584 by the other diffusive schemes. This is substantiated by the near-surface spectra (averaged
 585 over days 250 to 1000) of energy, enstrophy, and vertical buoyancy flux, shown in figure 9. In
 586 particular, a larger dissipation when compared to W9V (1) damps the baroclinic instability
 587 as seen by the drop in $w'b'$ and (2) inhibits the transfer of energy to larger scales resulting
 588 in weaker large-scale flows (see the energy spectra in figure 9). Interestingly, despite the
 589 numerical similarity, there's a marked difference between W9V and W9D, demonstrating
 590 the critical importance of selecting an appropriate smoothness measure when employing
 591 WENO-based reconstruction within the rotational framework. While the kinetic energy
 592 plots exhibit significant differences between schemes and resolutions, the disparity isn't as
 593 pronounced in the eddy APE. However, in the lowest resolution dispersive cases, strong
 594 explicit energy dissipation inhibits the development of baroclinic instability by mitigating
 595 meridional velocity fluctuations. Consequently, there's a discernible effect on the eddy APE,
 596 which consistently remains lower compared to other solutions.

597 To judge the “effective” resolution of the different approaches we look at zonal mean
 598 buoyancy averaged between 250 and 1000 days. The final buoyancy slope is determined
 599 by a balance between the mean buoyancy restoring, forcing the system towards the initial
 600 low-stratification jet state, and mesoscale eddies which tend to restratify the system. We
 601 expect a larger stratification for cases that can maintain higher levels of eddy kinetic energy
 602 as the equilibrium is pushed toward a lower APE state. Figure 10 shows mean buoyancy
 603 contours for the different cases compared to W9V, where the filled contours show QG2
 604 (top left), SM2 (top right), W9D (bottom left), and UP3 (bottom right) at 3.5-kilometer
 605 resolution, respectively. Figure 10 shows that, indeed, an increase in resolution leads to
 606 a more strongly stratified buoyancy profile, with W9V having a larger stratification than
 607 all the other cases, in virtue of the larger EKE expressed by the model. Notably, the
 608 W9V buoyancy contours at 7-kilometer resolution are practically indistinguishable from
 609 the buoyancy contours of the other cases at 3.5-kilometer resolution, suggesting a similarly
 610 resolved mesoscale eddy field. Stratification for the W9V case at 3.5-kilometer resolution
 611 (not shown), is slightly larger than the other cases at 3.5-kilometer resolution indicating that
 612 convergence is still not achieved at 3.5 kilometers. However, convergence in this case is not
 613 expected, given that the deformation radius is only 6.75 kilometers. Achieving full conversion

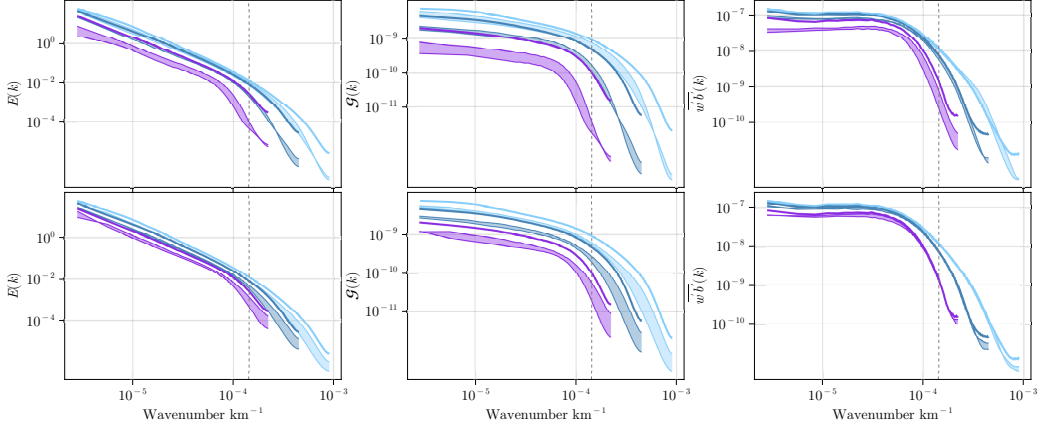


Figure 9. Time-averaged zonal energy spectra (left), enstrophy spectra (center), and $w'b'$ cospectra (right) averaged over the top 200 meters. The solid lines are W9V at 14 km (blue), 7 km (steel blue), and 3.5 km resolution (light blue). The banded lines of the same colors show the maximum and minimum trajectory for the dispersive cases (top: SM2, QG2) and diffusive schemes (bottom: UP3, W9D). The vertical dashed line shows the deformation radius.

at this resolution would probably require a representation of the inverse energy cascade through a backscattering parameterization. This test case in a more complex mesoscale turbulence simulation confirms that the W9V method achieves a higher “effective” resolution compared to the other test cases.

6 Summary and Conclusions

We introduced a new momentum advection scheme for the rotational form of the primitive equation based on the WENO reconstruction of fluxed variables (vorticity, horizontal divergence, and kinetic energy gradient). We constructed the new momentum advection scheme as an alternative to using oscillatory advection schemes paired with explicit viscous closures, taking inspiration from “implicit” large eddy simulation. We achieved this by (i) rewriting the primitive equations to expose both vorticity and horizontal divergence, (ii) implementing a diffusive reconstruction of fluxed variables (vorticity, horizontal divergence, and kinetic energy gradient), and (iii) choosing smoothness indicators for the WENO scheme that reduce the energy dissipation inherent in the method.

We found that our proposed WENO scheme outperforms the Leith closure in decaying homogeneous two-dimensional turbulence across a broader range of resolutions. The scheme performed well also in an idealized “eddy-permitting” setting when compared to other approaches typically used in ocean modeling. Importantly, the scheme does not require any calibration of unknown coefficients, but rather it adjusts to varying resolutions attaining an intrinsic “scale-awareness”.

By design the novel scheme significantly reduces dissipation, while efficiently removing variance at the grid-scale. We demonstrated that solutions obtained with our scheme are highly energetic and free from dispersive artifacts – a combination that has proven challenging to attain in “eddy-permitting” ocean flow regimes. In summary, our approach achieves a noise-free higher “effective” resolution when compared to the other dissipation approaches tested in this manuscript. The advantage of a higher “effective” resolution must be weighed against the additional cost of a numerical method involving high-order reconstruction stencils. In our GPU-based implementation, the W9V scheme in the idealized three-dimensional setting is only 20% more expensive than the most economical approach (UP3), while it has the same cost as the more complicated explicit closures (SM2 and QG2).

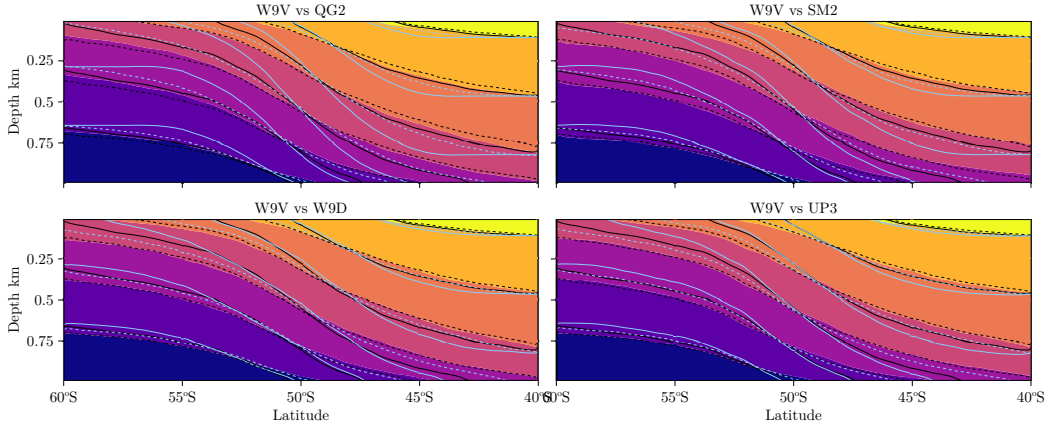


Figure 10. Left: Time and zonally averaged buoyancy for the different cases when compared to W9V. The filled contour shows the results of the comparative case (not W9V) at 3.5-kilometer resolution, acting as a reference, while the dashed and solid contours show solutions at 7 and 14-kilometer resolution, respectively. Black contours are the W9V case, while the light blue show the other case mentioned in the title of each frame (top left: QG2, top right: SM2, bottom left: W9D, bottom right: UP3).

We conclude by illustrating that the W9V advection scheme shows promise when implemented in an “eddy-permitting” near-global ocean model. The simulation is performed on a latitude-longitude grid with a horizontal resolution of 1/12-th of a degree spanning from 75°S to 75°N, 100 vertical levels, and realistic topography. The model is initialized from rest with temperature and salinity fields obtained from the data-constrained ECCO state estimate version 4 (Forget et al., 2015). The heat and salt fluxes are computed by restoring to the ECCO surface temperature and salinity fields. The surface wind stress is also taken from ECCO. The simulation is run for ten years with a time step of 270 seconds. The W9V method results in a stable and noise-free solution at the same computational cost of the QGLeith method, with the major advantage of requiring no tuning of parameters like a viscosity coefficient. Figure 1 shows the surface kinetic energy for the Gulf Stream and the Kuroshio current regions on March 1st, after 5 years of integration. The solution is characterized by vigorous turbulence that comprises of a web of frontal currents, without any signature of grid-scale noise. This near-global solution is only intended to showcase the feasibility of the proposed advection scheme in a realistic “eddy-permitting” ocean simulation. A detailed analysis of the accuracy of the solution is left for future work.

660 Appendix A Explicit closures used throughout the manuscript

661 Two-dimensional Leith closure

The Leith closure is specifically designed for two-dimensional turbulence, where enstrophy undergoes a forward cascade and is removed at small scales by viscous dissipation. The explicit form of the effective viscosity is derived from spectral scaling arguments, where the scaling of the Kolmogorov wavenumber in two-dimensional isotropic homogeneous turbulence follows (Kraichnan, 1967). A series of assumptions on the shape of the spectral slope lead to an explicit eddy viscosity of the following form (Leith, 1996):

$$668 \quad \nu_* = \left(\frac{\mathbb{C} \Delta}{\pi} \right)^3 |\nabla \zeta|, \quad (A1)$$

669 where \mathbb{C} is a tunable parameter of order 1.

670 Quasi-Geostrophic (QG) Leith closure

Building upon the principles of the original Leith subgrid-scale model, the quasi-geostrophic (QG) Leith model (Bachman et al., 2017; Pearson et al., 2017), expands its applicability specifically to the simulation of geophysical flows. Unlike the original Leith model, the QG Leith model accounts for the peculiar characteristics of geophysical turbulence, where potential vorticity, instead of two-dimensional vorticity, undergoes a forward cascade. To account for this difference, Bachman et al. (2017) propose to substitute the gradient of vertical vorticity in equation (A1) with the gradient of potential vorticity. Where quasi-geostrophic dynamics do not hold (e.g. on the equator or in mixed layers), the closure reverts to the classical two-dimensional Leith formulation. The effective viscosity in the QG Leith formulation is expressed by

$$\nu_* = \left(\frac{\mathbb{C}\Delta}{\pi} \right)^3 \left(\min(|\nabla q_1|, |\nabla q_2|, |\nabla q_3|)^2 + |\nabla(\nabla \cdot u)|^2 \right)^{1/2}, \quad (\text{A2})$$

where

$$\nabla q_1 = \nabla q + \partial_z \left(\frac{f}{N^2} \nabla b \right), \quad \nabla q_2 = \nabla q \left(1 + \frac{1}{\text{Bu}} \right), \quad \nabla q_3 = \nabla q \left(1 + \frac{1}{\text{Ro}^2} \right), \quad (\text{A3})$$

and $\nabla q = \nabla(\zeta + f)$. Bu and Ro above are the grid-scale Burger and Rossby numbers,

$$\text{Bu} \stackrel{\text{def}}{=} \frac{\Delta^2}{L_d^2} \text{ and } \text{Ro} \stackrel{\text{def}}{=} \frac{V}{|f|\Delta}, \quad (\text{A4})$$

where V is a velocity scale (here assumed to be equal to 1)

Smagorinsky closure

The “Smagorinsky” based closure we used here is the OM4p25 lateral friction closure (Adcroft et al., 2019), a combination of a laplacian and a bilaplacian dissipation, with the viscosity calculated as a maximum between a static viscosity and a “Smagorinsky” type viscosity (Smagorinsky, 1963). Specifically,

$$\nu_{4,*} = \max \left[\mathbb{C}_4 (D_s^2 + D_t^2)^{0.5} \Delta^4, \mathbb{C}_4^u \Delta^3 \right], \quad (\text{A5})$$

$$\nu_{2,*} = \max \left[\mathbb{C}_2 (D_s^2 + D_t^2)^{0.5} \Delta^2, \mathbb{C}_2^u \Delta \right] \mathbb{F}, \quad (\text{A6})$$

where $\nu_{4,*}$ and $\nu_{2,*}$ are the bilaplacian and the laplacian viscosity, respectively, and

$$D_s = \partial_x u - \partial_y v, \quad D_t = \partial_x v + \partial_y u. \quad (\text{A7})$$

Finally, $\mathbb{F} = (1 + 0.25\text{Bu}^{-2})^{-1}$ reduces the Laplacian viscosity where the deformation radius is resolved, and the value of the free parameters is

$$\mathbb{C}_4 = 0.06, \quad \mathbb{C}_4^u = 0.01, \quad \mathbb{C}_2 = 0.15, \quad \mathbb{C}_2^u = 0.01. \quad (\text{A8})$$

688

Appendix B Divergence flux, conservative vertical advection form

We set out to demonstrate that in terms of discrete kinetic energy conservation, \mathcal{V} is equivalent to $\mathcal{C} + \mathcal{D}$, or more specifically,

$$\sum_{i,j,k} (u \mathcal{V}_u \mathcal{V}_u + v \mathcal{V}_v \mathcal{V}_v) = \sum_{i,j,k} [u \mathcal{V}_u (\mathcal{C}_u + \mathcal{D}_u) + v \mathcal{V}_v (\mathcal{C}_v + \mathcal{D}_v)]. \quad (\text{B1})$$

690 Note that the influence of boundary fluxes is not taken into account in the following derivation.
691 Given two fields ϕ and ψ defined on a staggered C-grid, centered second-order reconstructions

and differences satisfy these pointwise properties (Adcroft et al., 1997)

$$\langle \psi \rangle^i \langle \phi \rangle^i = \langle \psi \phi \rangle^i - \frac{1}{4} \delta_i \psi \delta_i \phi , \quad (\text{B2})$$

$$\langle \delta_i \psi \rangle^i = \delta_i \langle \psi \rangle^i , \quad (\text{B3})$$

$$\left\langle \langle \psi \rangle^i \phi \right\rangle^i = \psi \langle \phi \rangle^i + \frac{1}{4} \delta_i (\phi \delta_i \psi) , \quad (\text{B4})$$

$$\delta_i (\langle \psi \rangle^i \phi) = \psi \delta_i \phi + \langle \phi \delta_i \psi \rangle^i , \quad (\text{B5})$$

and these integral properties (Madec et al., 2022)

$$\sum_i \psi \langle \phi \rangle^i = \sum_i \langle \psi \rangle^i \phi , \quad (\text{B6})$$

$$\sum_i \langle \psi \phi \rangle^i = \sum_i \psi \phi . \quad (\text{B7})$$

Note that the volumes associated with variables ϕ and ψ (denoting the “location” of the two quantities) are implied and not explicitly indicated. Combining (B6) with (B7) and (B2), we can derive an additional integral property

$$\sum_i \psi \left\langle \langle \phi \rangle^i \right\rangle^i = \sum_i \psi \phi - \frac{1}{4} \sum_i \delta_i \psi \delta_i \phi . \quad (\text{B8})$$

Focusing on the vertical advection term in the x-momentum equation (\mathcal{V}_u) and using property (B5):

$$\sum_{i,j,k} u \mathcal{V}_u \frac{\left\langle \langle W \rangle^i \delta_k u \right\rangle^k}{\mathcal{V}_u} = \underbrace{\sum_{i,j,k} u \mathcal{V}_u \frac{\left\langle \delta_k \left\langle \langle W \rangle^i \right\rangle^k u \right\rangle^k}{\mathcal{V}_u}}_{\text{term 1}} - \underbrace{\sum_{i,j,k} u \mathcal{V}_u \frac{\left\langle \left\langle u \delta_k \langle W \rangle^i \right\rangle^k \right\rangle^k}{\mathcal{V}_u}}_{\text{term 2}} . \quad (\text{B9})$$

Applying property (B3) followed by (B4) to term 1:

$$\text{term 1} = \sum_{i,j,k} u \mathcal{V}_u \underbrace{\frac{\delta_k \langle W \rangle^i \langle u \rangle^k}{\mathcal{V}_u}}_{\mathcal{C}_u} - \frac{1}{4} \sum_{i,j,k} u \delta_k \left(\delta_k \left(u \langle D \rangle^i \right) \right) . \quad (\text{B10})$$

where we made use of the discrete incompressibility condition ($D = -\delta_k W$). Applying the same incompressibility condition to term 2 followed by (B3) and (B8) yields

$$\text{term 2} = \sum_{i,j,k} u \mathcal{V}_u \underbrace{\frac{u \langle D \rangle^i}{\mathcal{V}_u}}_{\mathcal{D}_u} - \frac{1}{4} \sum_{i,j,k} (\delta_k u) \delta_k \left(u \langle D \rangle^i \right) . \quad (\text{B11})$$

Combining the two terms:

$$\sum_{i,j,k} u \mathcal{V}_u \mathcal{V}_u = \sum_{i,j,k} u \mathcal{V}_u (\mathcal{C}_u + \mathcal{D}_u) \quad (\text{B12})$$

$$- \frac{1}{4} \sum_{i,j,k} \left(u \delta_k (\delta_k (u \langle D \rangle^i)) + (\delta_k u) \delta_k (u \langle D \rangle^i) \right) . \quad (\text{B13})$$

Focusing on the second term on the RHS, using property (B7) on the second element in the summation yields

$$\sum_{i,j,k} u \mathcal{V}_u \mathcal{V}_u = \sum_{i,j,k} u \mathcal{V}_u (\mathcal{C}_u + \mathcal{D}_u) \quad (\text{B14})$$

$$- \frac{1}{4} \sum_{i,j,k} \left(u \delta_k (\delta_k (u \langle D \rangle^i)) + \left\langle (\delta_k u) \delta_k (u \langle D \rangle^i) \right\rangle^k \right) . \quad (\text{B15})$$

719 The second term on the RHS can now be reduced using (B5), where $\psi = u$ and $\phi =$
 720 $\delta_k(u \langle D \rangle^i)$, leading to

$$721 \sum_{i,j,k} u \mathcal{V}_u \mathcal{V}_u = \sum_{i,j,k} u \mathcal{V}_u (\mathcal{C}_u + \mathcal{D}_u) - \frac{1}{4} \sum_{i,j,k} \delta_k \left(u \left\langle \delta_k \left(u \langle D \rangle^i \right) \right\rangle^k \right), \quad (B16)$$

722 where the second term is the divergence of a vertical flux and, as such, its integral in the
 723 domain is equal to zero, leaving

$$724 \sum_{i,j,k} u \mathcal{V}_u \mathcal{V}_u = \sum_{i,j,k} u \mathcal{V}_u (\mathcal{C}_u + \mathcal{D}_u). \quad (B17)$$

725 The same can be done for the v component leading to (B1).

726 Appendix C Upwinding of the discrete horizontal divergence

727 Contrary to vorticity reconstruction, straightforward upwinding of the horizontal diver-
 728 gence might not always lead to a decrease in discrete kinetic energy. To demonstrate this,
 729 we consider a first-order upwind reconstruction, for which

$$730 u \{c\}^i = u \langle c \rangle^i - \frac{|u|}{2} \delta_i c. \quad (C1)$$

731 With the above reconstruction scheme, the discrete divergence flux is

$$732 u \frac{\{D\}^i}{\mathcal{V}_u} \hat{\mathbf{i}} + v \frac{\{D\}^j}{\mathcal{V}_v} \hat{\mathbf{j}} = \underbrace{\mathcal{D}_i \hat{\mathbf{i}} + \mathcal{D}_j \hat{\mathbf{j}}}_{\text{energy conserving}} - \underbrace{\left(|u| \frac{\delta_i D}{2 \mathcal{V}_u} \hat{\mathbf{i}} + |v| \frac{\delta_j D}{2 \mathcal{V}_v} \hat{\mathbf{j}} \right)}_{\text{not energy conserving}}. \quad (C2)$$

733 The associated change in discrete integrated kinetic energy reads

$$734 \partial_t \sum_{i,j,k} (u^2 \mathcal{V}_u + v^2 \mathcal{V}_v + w^2 \mathcal{V}_w) = \quad (C3)$$

$$735 = \underbrace{\sum_{i,j,k} (u|u|\delta_i \delta_i U + v|v|\delta_j \delta_j V)}_{\text{negative definite}} + \sum_{i,j,k} (u|u|\delta_i \delta_j V + v|v|\delta_j \delta_i U), \quad (C4)$$

736 where D has been divided into its two components ($\delta_i U$ and $\delta_j V$). Using (B5), we can show
 737 that the first term on the RHS is negative definite:

$$739 u|u|\delta_i \delta_i U = \delta_i \left(\langle u|u| \rangle^i \delta_i U \right) - \langle u|\delta_i U \delta_i u \rangle^i - \langle u \delta_i U \delta_i |u| \rangle^i, \quad (C5)$$

740 where the first term is the divergence of a flux and, provided that the discrete areas do not
 741 change drastically in neighboring cells,

$$742 u \delta_i U \delta_i |u| = |u| \delta_i U \delta_i u \geq 0. \quad (C6)$$

743 The same can be shown for $v|v|\delta_j \delta_j V$. Assuming that horizontally divergent motions are
 744 small

$$745 \delta_i U \sim -\delta_j V, \quad (C7)$$

746 the second term on the RHS of (C4) is

$$747 \sum_{i,j,k} (u|u|\delta_i \delta_j V + v|v|\delta_j \delta_i U) \sim - \sum_{i,j,k} (u|u|\delta_i \delta_i U + v|v|\delta_j \delta_j V), \quad (C8)$$

748 which is positive definite and counteracts the energy dissipation provided by the first term
 749 on the RHS of (C4). As such, upwinding the discrete divergence might have the undesired
 750 effect of injecting energy at the grid scale instead of removing it. To avoid adding kinetic
 751 energy at the grid scale, we apply a diffusive reconstruction only to the terms that lead to
 752 discrete energy dissipation (where the reconstruction direction is the same as the difference
 753 direction) while maintaining a centered reconstruction for the terms that could lead to energy
 754 production (where reconstruction and difference directions are perpendicular).

755 **Open Research Section**

756 The momentum advection scheme described in this paper is implemented in Oceanani-
 757 gans.jl (Ramadhan et al., 2020) starting from version 0.84.0. Visualizations were made using
 758 Makie.jl (Danisch & Krumbiegel, 2021). Scripts for reproducing and visualizing the idealized
 759 baroclinic setups are available at github.com/simone-silvestri/BaroclinicAdjustment.jl.
 760

761 **Acknowledgments**

762 Our work is supported by the generosity of Eric and Wendy Schmidt by recommendation of
 763 the Schmidt Futures program and by the National Science Foundation grant AGS-1835576.
 764 N.C.C. is supported by the Australian Research Council DECRA Fellowship DE210100749.
 765 We would also like to acknowledge the three anonymous reviewers and the handling editor
 766 for their constructive input that greatly improved the manuscript.

767 **References**

- 768 Adcroft, A., Anderson, W., Balaji, V., Blanton, C., Bushuk, M., Dufour, C., ... Zhang,
 769 R. (2019). The gfdl global ocean and sea ice model om4.0: Model description and
 770 simulation features. *Journal of Advances in Modeling Earth Systems*, 11(10), 3167-3211.
 771 doi: <https://doi.org/10.1029/2019MS001726>
- 772 Adcroft, A., Hill, C., & Marshall, J. (1997). Representation of topography by shaved cells in
 773 a height coordinate ocean model. *Monthly Weather Review*, 125(9), 2293-2315. doi:
 774 10.1175/1520-0493(1997)125<2293:ROTBSC>2.0.CO;2
- 775 Arakawa, A. (1966). Computational design for long-term numerical integration of the
 776 equations of fluid motion: Two-dimensional incompressible flow. Part I. *Journal of
 777 Computational Physics*, 1(1), 119-143. doi: 10.1016/0021-9991(66)90015-5
- 778 Arakawa, A., & Lamb, V. (1977). Computational design of the basic dynamical processes of
 779 the UCLA general circulation model. In J. Chang (Ed.), *General circulation models of
 780 the atmosphere* (Vol. 17, p. 173-265). Elsevier. doi: 10.1016/B978-0-12-460817-7.50009
 781 -4
- 782 Bachman, S., Fox-Kemper, B., & Pearson, B. (2017). A scale-aware subgrid model for
 783 quasi-geostrophic turbulence. *Journal of Geophysical Research: Oceans*. doi: 10.1002/
 784 2016JC012265
- 785 Balsara, D., & Shu, C. (2000). Monotonicity preserving weighted essentially non-oscillatory
 786 schemes with increasingly high order of accuracy. *Journal of Computational Physics*,
 787 160(2), 405-452. doi: 10.1006/jcph.2000.6443
- 788 Bates, J. R., & McDonald, A. (1982). Multiply-upstream, semi-Lagrangian advective schemes:
 789 Analysis and application to a multi-level primitive equation model. *Monthly Weather
 790 Review*, 110(12), 1831-1842. doi: 10.1175/1520-0493(1982)110<1831:MUSLAS>2.0
 791 .CO;2
- 792 Danisch, S., & Krumbiegel, J. (2021). Makie.jl: Flexible high-performance data visualization
 793 for Julia. *Journal of Open Source Software*, 6(65), 3349. doi: 10.21105/joss.03349
- 794 Ding, M., Liu, H., Lin, P., Meng, Y., Zheng, W., An, B., ... Chen, K. (2022). A century-long
 795 eddy-resolving simulation of global oceanic large- and mesoscale state. *Scientific Data*,
 796 9(1), 691. doi: 10.1038/s41597-022-01766-9
- 797 Fenty, I., & Wang, O. (2020). *ECCO geometry parameters for the Lat-Lon-Cap 90 (llc90)
 798 native model grid (version 4 release 4)*. NASA Physical Oceanography Distributed
 799 Active Archive Center. Retrieved from [https://podaac.jpl.nasa.gov/dataset/
 800 ECCO_L4_GEOMETRY_LLCC0090GRID_V4R4](https://podaac.jpl.nasa.gov/dataset/ECCO_L4_GEOMETRY_LLCC0090GRID_V4R4) doi: 10.5067/ECL5A-GRD44
- 801 Forget, G., Campin, J.-M., Heimbach, P., Hill, C., Ponte, R., & Wunsch, C. (2015).
 802 ECCO version 4: an integrated framework for non-linear inverse modeling and global
 803 ocean state estimation. *Geoscientific Model Development*, 8(10), 3071–3104. doi:
 804 10.5194/gmd-8-3071-2015

- Fox-Kemper, B., & Menemenlis, D. (2004). Can large eddy simulation techniques improve mesoscale rich ocean models? In M. Hecht & H. Hasumi (Eds.), *Ocean modeling in an eddying regime* (pp. 319 – 337). doi: 10.1029/177GM19
- Gent, P., & Mcwilliams, J. (1990). Isopycnal mixing in ocean circulation models. *Journal of Physical Oceanography*, 20(1), 150-155. doi: 10.1175/1520-0485(1990)020<0150: IMIOCM>2.0.CO;2
- Hahn, S., & Iaccarino, G. (2008). Simulations of vortex-dominated flows: adaptive vorticity confinement vs. rotational-form upwinding. *Center for Turbulence Research, Annual Research Brief*.
- Harten, A., Engquist, B., Osher, S., & Chakravarthy, S. (1987). Uniformly high order accurate essentially non-oscillatory schemes, III. *Journal of Computational Physics*, 71(2), 231-303. doi: 10.1016/0021-9991(87)90031-3
- Holland, W., Chow, J., & Bryan, F. (1998). Application of a third-order upwind scheme in the NCAR ocean model. *Journal of Climate*, 11(6), 1487-1493. doi: 10.1175/1520-0442(1998)011<1487:AOATOU>2.0.CO;2
- Ishiko, K., Ohnishi, N., Ueno, K., & Sawada, K. (2009). Implicit large eddy simulation of two-dimensional homogeneous turbulence using weighted compact nonlinear scheme. *Journal of Fluids Engineering*. doi: 10.1115/1.3077141
- Karaca, M., Lardjane, N., & Fedioun, I. (2012). Implicit large eddy simulation of high-speed non-reacting and reacting air/H₂ jets with a 5th order WENO scheme. *Computers & Fluids*, 62, 25-44. doi: 10.1016/j.compfluid.2012.03.013
- Kraichnan, R. (1967). Inertial ranges in two-dimensional turbulence. *The Physics of Fluids*, 10(7), 1417-1423. doi: 10.1063/1.1762301
- Leith, C. (1996). Stochastic models of chaotic systems. *Physica D: Nonlinear Phenomena*, 98(2), 481-491. (Nonlinear Phenomena in Ocean Dynamics) doi: 10.1016/0167-2789(96)00107-8
- Li, Y., Liu, H., Ding, M., Lin, P., Yu, Z., Yu, Y., ... Wang, P. (2020). Eddy-resolving simulation of cas-licom3 for phase 2 of the ocean model intercomparison. *Project. Adv. Atmos. Sci.*, 37, 1067 – 1080. doi: <https://doi.org/10.1007/s00376-020-0057-z>
- Madec, G., Bourdallé-Badie, R., Chanut, J., Clementi, E., Coward, A., Ethé, C., ... Moulin, A. (2022, March). *NEMO ocean engine*. Zenodo. doi: 10.5281/zenodo.6334656
- Madec, G., & Imbard, M. (1996). A global ocean mesh to overcome the North pole singularity. *Climate Dynamics*, 12, 381-388. doi: 10.1007/BF00211684
- Maulik, R., & San, O. (2018). Explicit and implicit LES closures for Burgers turbulence. *Journal of Computational and Applied Mathematics*, 327, 12-40. doi: 10.1016/j.cam.2017.06.003
- Mohammadi-Aragh, M., Klingbeil, K., Brüggemann, N., Eden, C., & Burchard, H. (2015). The impact of advection schemes on lateral shear and baroclinic instabilities. *Ocean Modelling*, 94, 112–127. doi: 10.1016/j.ocemod.2015.07.021
- Norman, M. R., Eldred, C., & Meena, M. G. (2023). Investigating inherent numerical stabilization for the moist, compressible, non-hydrostatic euler equations on collocated grids. *Journal of Advances in Modeling Earth Systems*, 15(10), e2023MS003732. doi: 10.1029/2023MS003732
- Osher, S., & Shu, C. (1991). High-order essentially nonoscillatory schemes for Hamilton–Jacobi equations. *SIAM Journal on Numerical Analysis*, 28(4), 907-922. doi: 10.1137/0728049
- Pearson, B., Fox-Kemper, B., Bachman, S., & Bryan, F. (2017). Evaluation of scale-aware subgrid mesoscale eddy models in a global eddy-rich model. *Ocean Modelling*, 115, 42-58. doi: 10.1016/j.ocemod.2017.05.007
- Pressel, K., Mishra, S., Schneider, T., Kaul, M., & Tan, Z. (2017). Numerics and subgrid-scale modeling in large eddy simulations of stratocumulus clouds. *Journal of Advances in Modeling Earth Systems*, 9(2), 1342-1365. doi: 10.1002/2016MS000778
- Ramadhan, A., Wagner, G. L., Hill, C., Campin, J.-M., Churavy, V., Besard, T., ... Ferrari, R. (2020). Oceananigans.jl: Fast and friendly geophysical fluid dynamics on GPUs. *The Journal of Open Source Software*, 4(44), 1965. doi: 10.21105/joss.01965

- 860 Ringler, T. D. (2011). Momentum, vorticity and transport: Considerations in the design
 861 of a finite-volume dynamical core. In P. Lauritzen, C. Jablonowski, M. Taylor, &
 862 R. Nair (Eds.), *Numerical techniques for global atmospheric models* (pp. 143–183).
 863 Berlin, Heidelberg: Springer Berlin Heidelberg. doi: 10.1007/978-3-642-11640-7_7
- 864 Ronchi, C., Iacono, R., & Paolucci, P. (1996). The “cubed sphere”: A new method for the
 865 solution of partial differential equations in spherical geometry. *Journal of Computational
 866 Physics*, 124(1), 93-114. doi: 10.1006/jcph.1996.0047
- 867 Roullet, G., & Gaillard, T. (2022). A fast monotone discretization of the rotating shallow
 868 water equations. *Journal of Advances in Modeling Earth Systems*. doi: 10.1029/
 869 2021MS002663
- 870 Schwarzkopf, F. U., Biastoch, A., Böning, C. W., Chanut, J., Durgadoo, J. V., Getzlaff,
 871 K., . . . Schubert, R. (2019). The inalt family – a set of high-resolution nests for the
 872 agulhas current system within global nemo ocean/sea-ice configurations. *Geoscientific
 873 Model Development*, 12(7), 3329–3355. Retrieved from <https://gmd.copernicus.org/articles/12/3329/2019/> doi: 10.5194/gmd-12-3329-2019
- 875 Shchepetkin, A., & McWilliams, J. (1998a). Quasi-monotone advection schemes based on
 876 explicit locally adaptive dissipation. *Monthly Weather Review*, 126(6), 1541-1580. doi:
 877 10.1175/1520-0493(1998)126<1541:QMASBO>2.0.CO;2
- 878 Shchepetkin, A., & McWilliams, J. C. (1998b). Quasi-monotone advection schemes based
 879 on explicit locally adaptive dissipation. *Monthly Weather Rev*, 126, 1541-1580.
- 880 Shu, C. (1997). *Essentially non-oscillatory and weighted essentially non-oscillatory schemes
 881 for hyperbolic conservation laws* (ICASE Report No. 97-65). Institute for Computer
 882 Applications in Science and Engineering, NASA Langley Research Center.
- 883 Silvestri, S., Wagner, G. L., Hill, C. N., Ardakani, M. R., Blaschke, J., Campin, J.-M., . . .
 884 Ferrari, R. (2023). Oceananigans.jl: A model that achieves breakthrough resolution,
 885 memory and energy efficiency in global ocean simulations.
 886 (arXiv:2309.06662) doi: 10.48550/arXiv.2309.06662
- 887 Smagorinsky, J. (1963). General circulation experiments with the primitive equations:
 888 I. the basic experiment. *Monthly Weather Review*, 91(3), 99-164. doi: 10.1175/
 889 1520-0493(1963)091<0099:GCEWTP>2.3.CO;2
- 890 Smolarkiewicz, P., & Margolin, L. (1998). MPDATA: A finite-difference solver for geophysical
 891 flows. *Journal of Computational Physics*, 140(2), 459-480. doi: 10.1006/jcph.1998.5901
- 892 Soufflet, Y., Marchesiello, P., Lemarié, F., Jouanno, J., Capet, X., Debreu, L., & Benshila,
 893 R. (2016). On effective resolution in ocean models. *Ocean Modelling*, 98, 36-50. doi:
 894 10.1016/j.ocemod.2015.12.004
- 895 Souza, A., He, J., Bischoff, T., Waruszewski, M., Novak, L., Barra, V., . . . Schneider, T.
 896 (2023). The flux-differencing discontinuous galerkin method applied to an idealized
 897 fully compressible nonhydrostatic dry atmosphere. *Journal of Advances in Modeling
 898 Earth Systems*, 15(4), e2022MS003527. doi: 10.1029/2022MS003527
- 899 Su, Z., Wang, J., Klein, P., Thompson, A., & Menemenlis, D. (2018). Ocean submesoscales
 900 as a key component of the global heat budget. *Nature Communications*, 9(1), 775. doi:
 901 <https://doi.org/10.1038/s41467-018-02983-w>
- 902 Sytine, I., Porter, D., Woodward, P., Hodson, S., & Winkler, K.-H. (2000). Convergence
 903 tests for the piecewise parabolic method and Navier–Stokes solutions for homogeneous
 904 compressible turbulence. *Journal of Computational Physics*, 158(2), 225-238. doi:
 905 10.1006/jcph.1999.6416
- 906 Vallis, G. K. (2017). *Atmospheric and oceanic fluid dynamics*. Cambridge University Press.
- 907 Van Leer, B. (1977). Towards the ultimate conservative difference scheme. IV. A new
 908 approach to numerical convection. *Journal of Computational Physics*, 23(3), 276-299.
 909 doi: 10.1016/0021-9991(77)90095-X
- 910 Woodward, P., & Colella, P. (1984). The numerical simulation of two-dimensional fluid
 911 flow with strong shocks. *Journal of Computational Physics*, 54(1), 115-173. doi:
 912 10.1016/0021-9991(84)90142-6
- 913 Zalesak, S. (1979). Fully multidimensional flux-corrected transport algorithms for fluids.
 914 *Journal of Computational Physics*, 31(3), 335-362. doi: 10.1016/0021-9991(79)90051-2

- 915** Zeng, K., Li, Z., Rana, Z., & Jenkins, K. (2021). Implicit large eddy simulations of turbulent
916 flow around a square cylinder at $Re=22,000$. *Computers & Fluids*, 226, 105000. doi:
917 10.1016/j.compfluid.2021.105000